

1 A 20-year (1998-2017) global sea surface dimethyl sulfide gridded 2 dataset with daily resolution

3 Shengqian Zhou¹, Ying Chen^{1,2,3}, Shan Huang^{4,5}, Xianda Gong^{6,7}, Guipeng Yang^{8,9,10}, Honghai Zhang^{8,9,10},
4 Hartmut Herrmann⁵, Alfred Wiedensohler⁵, Laurent Poulain⁵, Yan Zhang^{1,2}, Fanghui Wang¹, Zongjun
5 Xu¹, Ke Yan¹

6 ¹Shanghai Key Laboratory of Atmospheric Particle Pollution Prevention, Department of Environmental Science & Engineering,
7 Fudan University, Shanghai, 200438, China

8 ²Institute of Eco-Chongming (IEC), National Observations and Research Station for Wetland Ecosystems of the Yangtze
9 Estuary, Shanghai, 200062, China

10 ³Institute of Atmospheric Sciences, Fudan University, Shanghai 200438, China

11 ⁴Institute for Environmental and Climate Research, Jinan University, Guangzhou, 511443, China

12 ⁵Leibniz Institute for Tropospheric Research, Leipzig, 04318, Germany

13 ⁶Research Center for Industries of the Future, Westlake University, Hangzhou, 310030, China

14 ⁷Key Laboratory of Coastal Environment and Resources of Zhejiang Province, School of Engineering, Westlake University,
15 Hangzhou, 310030, China

16 ⁸Frontiers Science Center for Deep Ocean Multispheres and Earth System, and Key Laboratory of Marine Chemistry Theory
17 and Technology, Ministry of Education, Ocean University of China, Qingdao, 266100, China

18 ⁹Laboratory for Marine Ecology and Environmental Science, Qingdao National Laboratory for Marine Science and
19 Technology, Qingdao, 266071, China

20 ¹⁰College of Chemistry and Chemical Engineering, Ocean University of China, Qingdao, 266100, China

21 *Correspondence to:* Ying Chen (yingchen@fudan.edu.cn)

22 **Abstract.** The oceanic emission of dimethyl sulfide (DMS) plays a vital role in the Earth's climate system and constitutes a
23 substantial source of uncertainty in evaluating aerosol radiative forcing. Currently, the widely used monthly climatology of
24 sea surface DMS concentration falls short of meeting the requirement for accurately simulating DMS-derived aerosols by
25 chemical transport models. Hence, there is an urgent need for a high-resolution, multi-year global sea surface DMS dataset.
26 Here we develop an artificial neural network ensemble model using 9 environmental factors as input features, which exhibits
27 high accuracy and generalization in predicting DMS concentrations. Subsequently, a global sea surface DMS concentration
28 and flux dataset ($1^\circ \times 1^\circ$) with daily resolution spanning from 1998 to 2017 is established. According to this dataset, the global
29 annual average concentration was ~ 1.72 nM, and the annual total emission was ~ 17.0 TgS yr⁻¹, with $\sim 61\%$ originating from
30 the southern hemisphere. While overall seasonal variations are consistent with previous DMS climatologies, notable
31 differences exist in regional-scale spatial distributions. The new dataset enables further investigations into daily and decadal
32 variations. Throughout the period 1998–2017, the global annual average concentration exhibited a slight decrease, while total
33 emissions showed no significant trend. The DMS flux from our dataset showed a stronger correlation with observed
34 atmospheric methanesulfonic acid concentration compared to those from previous monthly climatologies. Therefore, it can
35 serve as an improved emission inventory of oceanic DMS and has the potential to enhance the simulation of DMS-derived

36 aerosols and associated radiative effects. The new DMS gridded products are available at <https://zenodo.org/records/10906101>
37 (Zhou et al., 2024).

38 **1 Introduction**

39 Dimethyl sulfide (DMS), primarily produced by ocean biota, accounts for more than half of natural sulfur emissions and
40 significantly contributes to sulfur dioxide in the troposphere (Sheng et al., 2015; Andreae, 1990), which can be oxidized to
41 sulfuric acid and form sulfate aerosols (Barnes et al., 2006; Hoffmann et al., 2016). Sulfate aerosols play an important role in
42 climate systems by scattering solar radiation, changing cloud condensation nuclei (CCN) population, and altering cloud
43 properties (Masson-Delmotte et al., 2021). Recent studies have proven that CCN over the remote ocean and polar regions are
44 primarily composed of non-sea-salt sulfate (nss-SO_4^{2-}) (Quinn et al., 2017; Park et al., 2021). Given the weak influence of
45 anthropogenic SO_2 over open oceans, marine biogenic DMS emerges as a crucial source of nss-SO_4^{2-} , regulating oceanic
46 climate (McCoy et al., 2015). Accordingly, DMS has been suggested to be the key substance in the postulated feedback loop
47 of marine phytoplankton to climate warming (the “CLAW” hypothesis) (Charlson et al., 1987), albeit facing several
48 controversies (Quinn and Bates, 2011). To accurately simulate the climate effects of DMS-derived aerosols, high-fidelity and
49 high-resolution data on sea surface DMS concentrations and emission fluxes are required, along with further exploration of
50 complex atmospheric chemical and physical processes (Hoffmann et al., 2016; Novak et al., 2021). It has been indicated that
51 the uncertainty in DMS emission flux is the second largest contributor to the overall uncertainty associated with natural
52 aerosols in evaluating the aerosol indirect radiative forcing (Carslaw et al., 2013). Therefore, understanding the spatiotemporal
53 variations of DMS in global oceans is currently an important task.

54 There are complex production and consumption mechanisms of DMS in the upper ocean, which makes it difficult to well
55 capture the dynamics and distributions of sea surface DMS across different regions. Dimethylsulfoniopropionate (DMSP), the
56 major precursor of DMS, is synthesized mainly by phytoplankton in the photic zone and plays a variety of physiological
57 functions in algal cells (Stefels, 2000; Sunda et al., 2002; McParland and Levine, 2018). The DMSP yield varies significantly
58 among algal species (Stefels et al., 2007; Keller et al., 1989), and DMS can be produced through DMSP intracellular and
59 extracellular cleavage by both algae and bacteria (Alcolombri et al., 2015; Zhang et al., 2019). Therefore, the oceanic DMS
60 produced via multiple pathways can be affected by many biotic and abiotic factors, including temperature, salinity, solar
61 radiation, mixed layer depth, nutrients, oxygen, acidity, etc. (Simó and Pedrós-Alió, 1999a; Vallina and Simó, 2007; Stefels,
62 2000; Zindler et al., 2014; Six et al., 2013; Omori et al., 2015; Stefels et al., 2007). In addition, seawater DMS undergoes
63 various removal pathways (bacterial consumption, photodegradation, sea-to-air ventilation, etc.), further complicating its
64 cycling (Stefels et al., 2007; Galí and Simó, 2015; Hopkins et al., 2023). Therefore, although previous studies have developed
65 several empirical algorithms (Simó and Dachs, 2002; Belviso et al., 2004b; Vallina and Simó, 2007) and process-embedded
66 prognostic models (Kloster et al., 2006; Vogt et al., 2010; Belviso et al., 2011; Wang et al., 2015) based on relevant variables

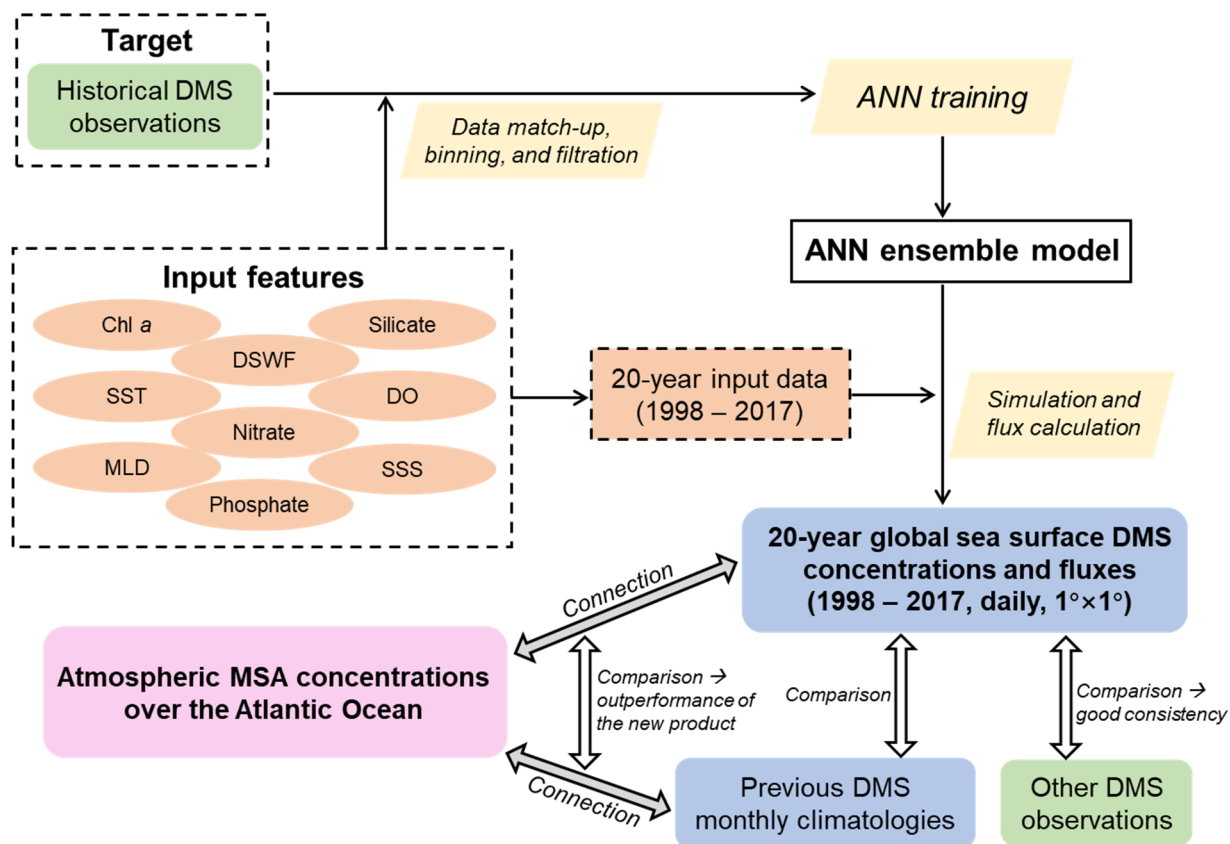
67 (mixed layer depth, chlorophyll *a*, nutrients, radiation, phytoplankton group, etc.) to estimate the distribution of DMS, their
68 results showed significantly different patterns and inconsistency with observations in many regions (Tesdal et al., 2016;
69 Belviso et al., 2004a). Recently, Galí et al. (2018) developed a new empirical algorithm following a parameterization of DMSP
70 (Galí et al., 2015). The estimated DMS field exhibited a generally higher consistency with observations than those derived
71 from previous algorithms SD02 (Simó and Dachs, 2002) and VS07 (Vallina and Simó, 2007), but this method did not consider
72 the influences of nutrients and still exhibited substantial biases in certain regions (e.g., near the Antarctic).

73 Since Lovelock et al. (1972) first discovered the ubiquitous presence of DMS in seawater, numerous observations of sea
74 surface DMS have been conducted worldwide, yielding a substantial volume of observational data to date. Based on these
75 worldwide measurements, monthly climatology of global DMS can be generated through interpolation and extrapolation
76 (Hulswar et al., 2022; Kettle et al., 1999; Lana et al., 2011). The latest version incorporated 873,539 raw observations (48,898
77 after data filtration and unification for climatology development), and the estimated global annual mean concentration and
78 total flux are 2.26 nM and 27.1 TgS yr⁻¹, respectively (Hulswar et al., 2022). However, despite the abundance of data,
79 significant spatial and temporal disparities persist, potentially introducing large uncertainties in regions or periods with sparse
80 observations. Furthermore, the observational data from different years within a particular month were combined together for
81 interpolation and extrapolation, and the interannual variations cannot be investigated by this approach.

82 In recent years, the application of data-driven approaches like machine learning to Earth system science has drawn more and
83 more attention. Compared with traditional approaches, machine learning explores larger function space and captures more
84 hidden information from the big data, hence it often provides a better prediction performance (Reichstein et al., 2019; Zheng
85 et al., 2020; Bergen et al., 2019). For instance, a recent study demonstrated that artificial neural network (ANN) can capture
86 much more (~66%) of the raw data variance than multilinear regression (~39%), and a global monthly climatology of sea
87 surface DMS concentration has been developed based on ANN model (Wang et al., 2020). The machine learning techniques
88 have also been used to simulate the distribution of DMS in the Arctic (Humphries et al., 2012; Qu et al., 2016), North Atlantic
89 Ocean (Bell et al., 2021; Mansour et al., 2023), Northeast Pacific Ocean (McNabb and Tortell, 2022), Southern Ocean
90 (McNabb and Tortell, 2023), and East Asia (Zhao et al., 2022).

91 However, to our best knowledge, there is currently no global-scale sea surface gridded DMS dataset with both high time
92 resolution (daily) and long-term coverage (> 10 years). Such a dataset is urgently needed for modeling the atmospheric
93 processes and climatic implications of oceanic DMS. The sea surface concentration and sea-to-air emission flux of DMS can
94 vary greatly from day to day (Simó and Pedrós-Alió, 1999b), and the emitted DMS exerts effects on the atmosphere over time
95 scales of several hours to days. Relying solely on monthly climatology of DMS as the emission inventory may fail to capture
96 important details and could lead to large modeling biases compared to observed concentrations of atmospheric DMS or its
97 oxidation products (Chen et al., 2018; Fung et al., 2022).

98 Here, we build a 20-year (1998 – 2017) global sea surface DMS gridded dataset ($1^\circ \times 1^\circ$) with a daily resolution based on a
 99 data-driven machine learning approach (ANN ensemble). This product can improve our understanding of the spatiotemporal
 100 variations of oceanic DMS. More importantly, it can serve as an updated emission inventory of marine biogenic DMS for
 101 chemical transport models, which is beneficial for enhancing the simulation of atmospheric processes of DMS and reducing
 102 the uncertainties in marine aerosol's climate effects. The paper consists of four main parts as depicted in Fig. 1: (1) the
 103 development of machine learning model based on global DMS measurements and 9 ancillary environmental variables; (2) the
 104 derived spatial and temporal distributions of DMS and comparisons with previous estimates; (3) an example showing the
 105 superiority of our newly developed DMS field through its correlation with atmospheric biogenic sulfur; and (4) the
 106 uncertainties and limitations inherent in our approach and the resulting data product.



107

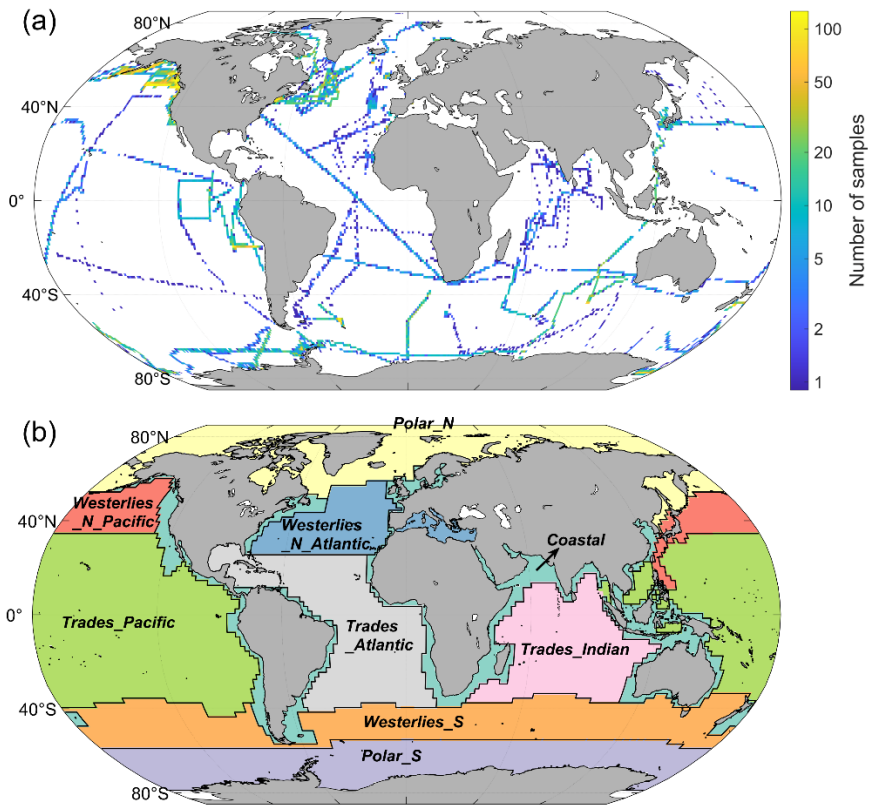
108 **Figure 1.** Flowchart of this study, including the development of ANN ensemble model, construction of new DMS gridded
 109 dataset, and subsequent evaluations of this product.

110 2 Methodology

111 2.1 Input datasets

112 The in-situ DMS measurement data used for training the machine learning model primarily sourced from the Global Surface
113 Seawater DMS (GSSD) database (Kettle et al., 1999). The GSSD database contains a total of 87,801 DMS measurements
114 collected across 266 cruise and fixed-site observation campaigns from 11 March 1972 to 27 August 2017
115 (<https://saga.pmel.noaa.gov/dms/>, last access: 1 April 2020). Hulswar et al. (2022) consolidated other DMS measurements not
116 included in the GSSD database to establish an updated DMS climatology. Here we incorporated these additional data predating
117 2017, originating from 8 campaigns (number of samples = 6,711). The spatial distribution of these combined 94,512 in-situ
118 observational data is shown in Fig. S1, which covers all major regions of the global ocean.

119 We selected 9 environmental variables relevant to DMS biogeochemical processes as input features, including chlorophyll *a*
120 (Chl *a*), sea surface temperature (SST), mixed layer depth (MLD), nitrate, phosphate, silicate, dissolved oxygen (DO),
121 downward short-wave radiation flux (DSWF), and sea surface salinity (SSS). The data sources and relevant information of
122 these 9 input variables and DMS are listed in Table 1. Chl *a* data were obtained from both in-situ observations, co-located with
123 DMS data, and satellite remote sensing products (Copernicus-GlobColour, Level-4, daily, $0.042^{\circ} \times 0.042^{\circ}$). The Copernicus-
124 GlobColour Level-4 dataset integrates multiple upstream sensors including SeaWiFS, MODIS-Aqua & Terra, MERIS, VIIRS-
125 SNPP & JPSS1, and OLCI-S3A & S3B, with an interpolation procedure applied to fill missing data (Garneison et al., 2019).
126 Daily SST data ($0.25^{\circ} \times 0.25^{\circ}$) were from the NOAA OI SST V2 high-resolution blended reanalysis dataset (Huang et al., 2021).
127 Daily MLD, DSWF, and SSS were from the modeling outputs of NASA's "Estimating the Circulation and Climate of the
128 Ocean" (ECCO) consortium, Version 4 Release 4 (V4r4) (Forget et al., 2015). The sea surface concentrations of nitrate,
129 phosphate, silicate, and DO were from the CMEMS global biogeochemical multi-year hindcast dataset (daily, $0.25^{\circ} \times 0.25^{\circ}$).
130 The surface wind speed (WS) and sea ice fraction (SI) data are needed in the calculation of sea-to-air flux (details are provided
131 in Section 2.4.2). Here we utilized the daily 10-meter WS data from ECCO V4r4 and the daily SI data from NOAA OI SST
132 V2. Since there are multiple different spatial grids among all datasets, the data match-up has been conducted as described in
133 the next section.



134

135 **Figure 2.** (a) The distribution of 41,157 DMS observational data after matchup, filtration, and binning for constructing the
 136 ANN model. The grid size is $1^\circ \times 1^\circ$. (b) Nine oceanic regions separated based on Longhurst's biomes (Longhurst, 1998).

137

138 **Table 1.** The data sources and related information of variables used for model development, DMS simulation, and flux
 139 calculation

Variable	Data source	URL	Temporal resolution	Temporal coverage	Spatial grid
DMS	GSSD database	https://saga.pmel.noaa.gov/dms/	In-situ	Mar. 1972 – Aug. 2017	-
	Other campaigns integrated in Hulswar et al. (2022)	https://data.mendeley.com/datasets/hyn62spny2/1	In-situ	Feb. 2000 – Jun. 2016	-
Chl <i>a</i>	GSSD database	https://saga.pmel.noaa.gov/dms/	In-situ	Oct. 1980 – Aug. 2017	-
	Copernicus-GlobColour Level-4	https://data.marine.copernicus.eu/product/OCEANCOLOUR_GLO_BGC_L4_MY_009_104/description	Daily	Sep. 1997 – present	0.042°×0.042°
	CMEMS global biogeochemical multi-year hindcast (only used for the simulation of DMS concentration in polar regions when satellite Chl <i>a</i> is unavailable)	https://data.marine.copernicus.eu/product/GLOBAL_MULTIYEAR_BGC_001_029/description	Daily	Jan. 1993 – present	0.25°×0.25°
SST	NOAA OI SST V2	https://psl.noaa.gov/data/gridded/data.noaa.oisst.v2.hires.html	Daily	Sep. 1981 – present	0.25°×0.25°
MLD					
DSWF	NASA ECCO V4r4	https://data.nas.nasa.gov/echo/data.php?dir=/eccodata/llc_90/ECCOV4/Release4	Daily	Jan. 1992 – Dec. 2017	LLC90 (22 – 110 km)
SSS					
Nitrate					
Phosphate	CMEMS global biogeochemical multi-year hindcast	https://data.marine.copernicus.eu/product/GLOBAL_MULTIYEAR_BGC_001_029/description	Daily	Jan. 1993 – present	0.25°×0.25°
Silicate					
DO					
WS	NASA ECCO V4r4	https://data.nas.nasa.gov/echo/data.php?dir=/eccodata/llc_90/ECCOV4/Release4	Daily	Jan. 1992 – Dec. 2017	LLC90 (22 – 110 km)
SI	NOAA OI SST V2	https://psl.noaa.gov/data/gridded/data.noaa.oisst.v2.hires.html	Daily	Sep. 1981 – present	0.25°×0.25°

140

141 2.2 Data preprocessing for model development

142 The data extraction and match-up were performed based on the sampling location and time associated with each DMS
 143 measurement record, as well as the temporal range and grid distribution of each variable. For satellite-retrieved Chl *a*, the data
 144 of the grids covering DMS sampling locations were extracted. If the data of the corresponding grid is missing, the average

145 value of the 5×5 grids nearby was calculated and used. For other variables, only values in the grids matching the DMS sampling
146 locations were extracted.

147 There are in-situ Chl *a* measurements co-located with certain GSSD data. They were also used along with satellite-retrieved
148 Chl *a*. In-situ Chl *a* measurements with low precision (defined as $< 0.1 \text{ mg m}^{-3}$, and the number of significant digits is 1) were
149 removed. For a specific in-situ observation campaign, if the number of low-precision values is larger than 10 and accounts for
150 more than half, all in-situ Chl *a* data from this campaign were excluded. In addition, the in-situ Chl *a* data in the GSSD database
151 were measured by two different methods: Turner fluorometry and high-performance liquid chromatography (HPLC). In order
152 to improve mutual consistency, a conversion between the data from these two methods was applied and then the in-situ Chl *a*
153 concentrations were adjusted to match up with satellite Chl *a* following the functions described in Galí et al. (2015). After that,
154 the statistical outliers for all $\log_{10}(\text{Chl } a)$ (outside the range of average ± 3 standard deviations) were eliminated. The
155 comparison between in-situ and satellite-retrieved Chl *a* data is shown in Fig. S2. A strong consistency between in-situ and
156 daily satellite Chl *a* data ($R^2 > 0.5$, $\text{RMSE} < 0.4$) suggests the rationale for integrating these datasets. The \log_{10} transformation
157 was applied to make the data distribution close to normal distribution. When finally selecting the $\log_{10}(\text{Chl } a)$ corresponding
158 to each DMS data, in-situ data were prioritized where available; otherwise, the satellite-retrieved data were used.

159 DMS and extracted MLD and three nutrients (nitrate, phosphate, silicate) were also performed \log_{10} transformation. The
160 statistical outliers of each variable were excluded as mentioned above. After data filtration, a total of 633,361 samples with
161 valid data for all variables were obtained. To avoid data aggregation bias stemming from multiple data points gathered within
162 a narrow temporal and spatial range (i.e., the same day and within a region smaller than $0.05^\circ \times 0.05^\circ$), these data points were
163 averaged. Consequently, 41,157 binned samples were utilized for subsequent model development, with their spatial
164 distribution depicted in Fig. 2a.

165 We divided the global ocean into 9 regions based on Longhurst's biomes (Longhurst, 1998). There are 6 biomes in Longhurst's
166 definition, including Coastal, Polar_N, Polar_S, Westerlies_N, Westerlies_S, and Trades (the .shp file of Longhurst's biomes
167 and provinces was downloaded from <https://www.marineregions.org/downloads.php#longhurst>). We further divided
168 Westerlies_N into Westerlies_N_Pacific and Westerlies_N_Atlantic, and divided Trades into Trades_Pacific, Trades_Indian,
169 and Trades_Atlantic by different oceanic basins, as shown in Fig. 2b. It is noteworthy that there are 11,237 samples in the
170 Coastal region, constituting 27.3% of the entire sample set, despite the Coastal biome accounting for only 9.7% of the global
171 ocean area. Given the distinct seawater physiochemical and biological conditions in coastal seas compared to other regions,
172 the disproportionately higher density of samples within the Coastal biome might cause the model to overly prioritize this region.
173 To mitigate this data imbalance and ensure the model captures broader patterns in open oceans, we adjusted the data
174 distribution during model training and validation processes. Specifically, we adjusted the fraction of coastal samples to match
175 the area fraction. Further details are provided in the subsequent section and visualized in Fig. 3a.

176 2.3 Artificial neural network training and validation

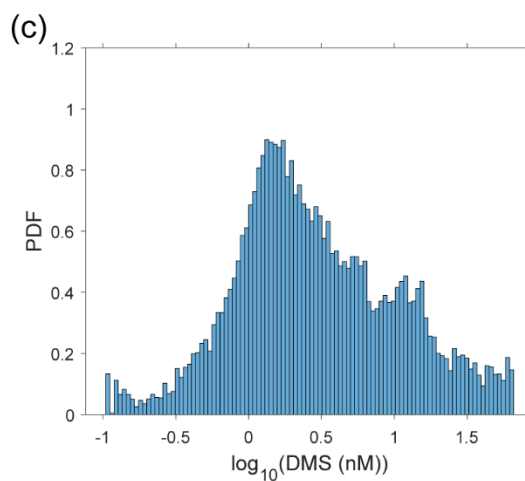
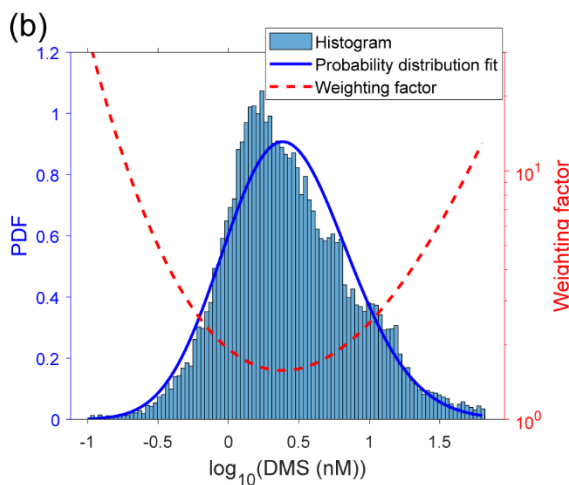
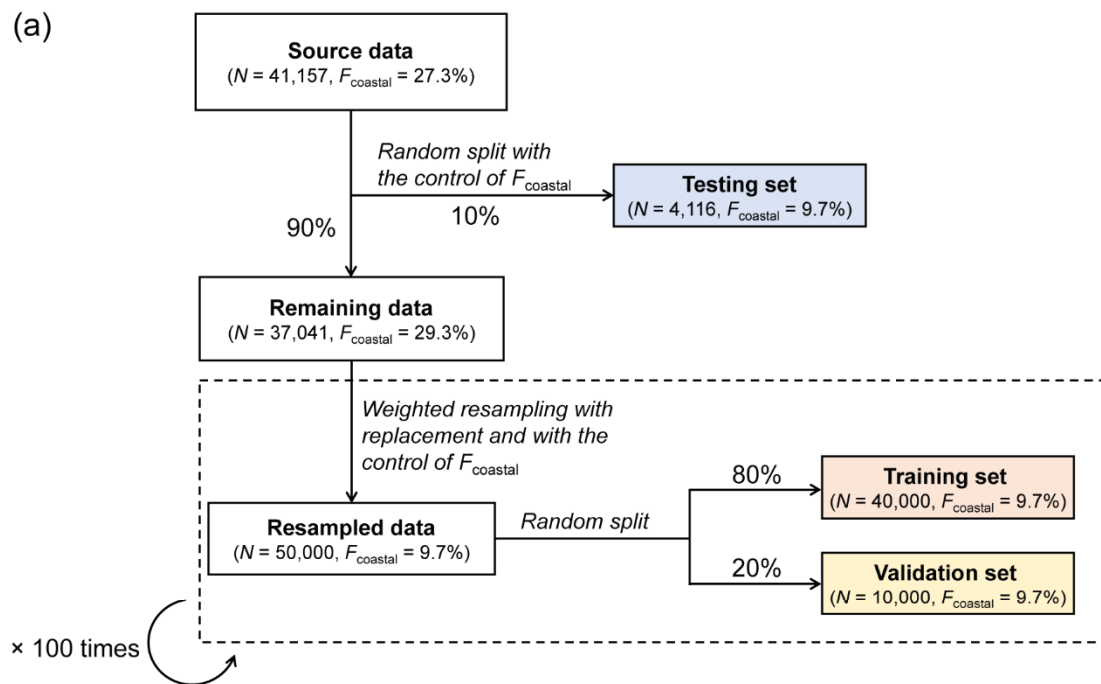
177 The 41,157 binned samples after the previously mentioned data preprocessing were used to develop the artificial neural
178 network (ANN) model. The target feature is $\log_{10}(\text{DMS})$, and the input features are $\log_{10}(\text{Chl } a)$, SST, $\log_{10}(\text{MLD})$,
179 $\log_{10}(\text{nitrate})$, $\log_{10}(\text{phosphate})$, $\log_{10}(\text{silicate})$, DO, DSWF, and SSS. The data of all variables were standardized before
180 training.

181 We randomly selected 10% of the samples ($n = 4,116$) to be entirely excluded from training, as a testing subset for global
182 validation and overfitting test. The testing subset was controlled to contain a proportion of coastal samples (denoted as F_{coastal})
183 at 9.7%. Specifically, 401 samples were randomly selected from Coastal biome, while 3,715 samples were selected from other
184 biomes to compose the testing subset. Then, the remaining samples ($n = 37,041$) were utilized for training and cross validation.
185 Apart from the data imbalance between coastal and non-coastal regions, there exists an imbalance across different DMS
186 concentration ranges. As shown in Fig. 3b, the majority of DMS concentration values (78.6%) fall within the range of 0.8 to
187 10 nM ($\log_{10}(\text{DMS})$ between -0.1 to 1). Samples with DMS concentrations exceeding 15 nM or falling below 0.3 nM only
188 represent 6.9% of the entire sample set. Here we implemented a weighted resampling strategy to mitigate this imbalance and
189 enhance the model's capability in predicting extreme values. We randomly sampled 50,000 samples with replacement from
190 the remaining sample set. The probability of each sample being selected is proportional to the weighting factor shown in Fig.
191 3b, which is dependent on its DMS concentration. Samples exhibiting high or low DMS concentration values are more likely
192 to be selected, whereas those with intermediate concentrations are less likely to be selected. The details of the weighting factor
193 are explained in Appendix B. We also controlled the F_{coastal} value of the resampled data equals to 9.7% by the same method as
194 described above, i.e., applying the resampling process to coastal and non-coastal samples separately and combining them
195 together afterwards. The data distribution of DMS concentrations after the resampling process is shown in Fig. 3c. The fraction
196 of samples with DMS concentrations above 15 nM or below 0.3 nM is elevated to 15.0%. The 50,000 samples were then
197 randomly split to a training set (80%) and a validation set (20%). Since there are duplicate samples in the resampled dataset,
198 the random data split was conducted based on the original sample ID before resampling to ensure that there was no sample
199 overlap between the training and validation sets.

200 Our feedforward fully connected neural network comprises two hidden layers, with 15 nodes in each layer. The activation
201 functions for the first and second layers are ReLU and tanh, respectively. We applied L2 regularization ($\lambda = 5\text{E-}4$) to
202 counteract overfitting. The loss function is mean square error (MSE). Training stops if the validation loss is greater than or
203 equal to the minimum validation loss computed so far 20 times in a row. The training processes were carried out with Statistics
204 and Machine Learning Toolbox on Matlab 2022b. We repeated the data resampling, split, and training processes for 100 times
205 and obtained 100 neural networks. The average prediction results of multiple ANNs shows a much higher consistency with
206 the observations than a single ANN (Fig. S3). As the number of ANNs (N_{training}) increases, the accuracy of model predictions
207 initially improves and then diminishes, eventually stabilizing. We adopted the average output of 10 ANNs as the final output,

208 balancing performance and computational costs effectively. This kind of multiple-training approach, often termed “ANN
 209 ensemble” or “Monte Carlo cross-validation”, has been widely used to improve the model generalization and performance
 210 (Sigmund et al., 2020; Holder et al., 2022) as well as get a better model evaluation (Dubitzky et al., 2007).

211



212

213 **Figure 3.** Data split and resampling strategy for ANN model training and testing. (a) Flowchart of the data split and resampling
 214 procedures. N and F_{coastal} denote the number of samples and the fraction of coastal samples, respectively. (b) The probability

215 distribution of raw $\log_{10}(\text{DMS})$ values and the relationship between the weighting factor for weighted resampling and
216 $\log_{10}(\text{DMS})$ value. PDF represents the probability density function. (c) The probability distribution of $\log_{10}(\text{DMS})$ values after
217 weighted resampling.

218 **2.4 Deriving the 20-year global DMS distributions**

219 **2.4.1 Simulation of sea surface DMS concentrations**

220 First, we constructed the daily gridded dataset of input variables with a spatial resolution of $1^\circ \times 1^\circ$ from 1998 to 2017 using
221 the data sources listed in Table 1 (except in-situ Chl *a* data). Datasets with a higher spatial resolution than $1^\circ \times 1^\circ$ were binned
222 into $1^\circ \times 1^\circ$. In polar regions, the satellite Chl *a* data are missing during winter, and the Chl *a* data from CMEMS global
223 biogeochemical multi-year hindcast were used to fill the missing values. Then, the obtained gridded dataset was fed into the
224 ANN ensemble model, and the 20-year global distribution of sea surface DMS concentration with daily resolution was
225 simulated.

226 **2.4.2 Calculation of sea-to-air fluxes**

227 The sea-to-air fluxes of DMS were calculated on the basis of simulated surface DMS concentrations following equation (1):

$$228 \quad DMS \text{ flux} = Kt \times \left(DMS_w - \frac{DMS_a}{H} \right) \quad (1)$$

229 Here DMS_w and DMS_a are DMS concentrations in surface seawater and air, respectively. H is Henry's law constant of DMS.

230 Since $\frac{DMS_a}{H}$ is usually $\ll DMS_w$, this term was omitted in the calculation. Kt is the total transfer velocity considering the sea
231 ice coverage fraction (SI):

$$232 \quad Kt = k_t \times (1 - SI) \quad (2)$$

233 k_t is the total transfer velocity without considering sea ice which is calculated by equation (3):

$$234 \quad \frac{1}{k_t} = \frac{1}{k_w} + \frac{1}{k_a \times H} \quad (3)$$

235 Here k_w and k_a are the water-side transfer velocity and air-side transfer velocity, respectively. We used the same approach as
236 Galí et al. (2019) to obtain k_w , k_a , and H for DMS, where the effect of wind speed was considered for k_a , and the influences of
237 SST and SSS were considered for H . The calculations of k_a and H followed the parameterizations of Johnson (2010). As for
238 k_w calculation, we adopted the bubble scheme (Woolf, 1997), which divided the sea-to-air mass transfer process into
239 turbulence- and bubble-mediated gas exchange. The calculated k_w based on the bubble scheme is lower than that of
240 Nightingale's scheme (Nightingale et al., 2000) under conditions of high wind speed, exhibiting a smaller deviation from the
241 actual value (Beale et al., 2014; Galí et al., 2019). Before calculation, WS and SI data were also binned by $1^\circ \times 1^\circ$ grid. By
242 using WS and SI together with SST and SSS datasets, we obtained the daily gridded Kt and then calculated the sea-to-air DMS
243 fluxes (daily, 1998–2017) by multiplying simulated DMS concentrations by Kt values.

245 **3.1 Model performance**

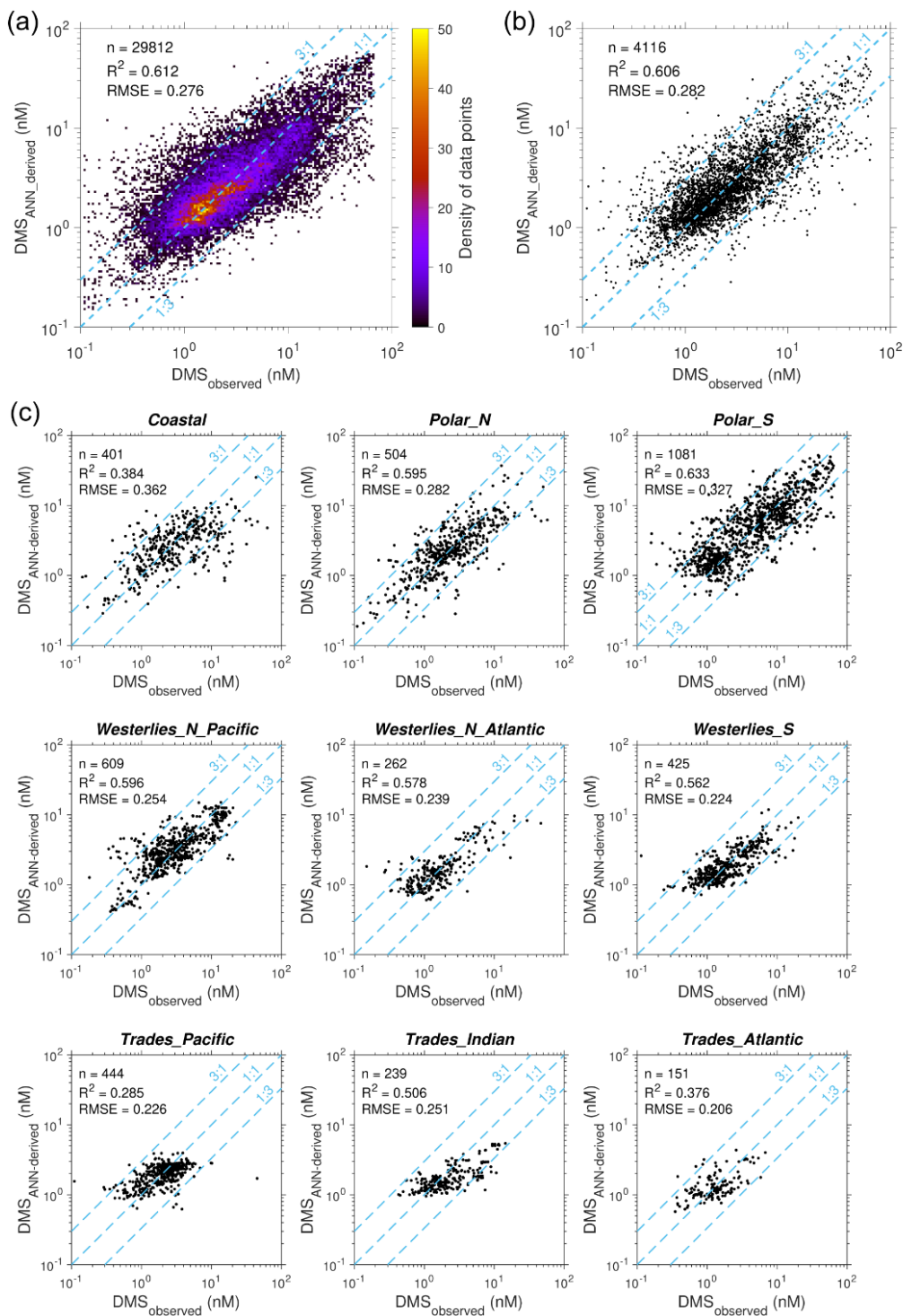
246 As shown in Fig. 4a, the newly developed ANN ensemble model captures a substantial part of data variance globally (\log_{10}
247 space $R^2 = 0.612$ and $RMSE = 0.276$). 91.6% of ANN simulated concentration values fall within 1/3 to 3 times of corresponding
248 true values. The performance for testing set ($R^2 = 0.606$, $RMSE = 0.282$, and 90.8% of data within the range of 1/3 to 3 times
249 of observations) is very close to that for the training dataset (Fig. 4b), suggesting no obvious overfitting. The ANN model
250 exhibits better performance compared to previous empirical and process-based models ($R^2 = 0.01\sim 0.14$) (Tesdal et al., 2016)
251 as well as the satellite-based algorithm ($R^2 = 0.50$) (Galí et al., 2018). The ANN model developed by Wang et al. (2020)
252 showed a slightly higher performance ($R^2 = 0.66$, $RMSE = 0.264$ for training dataset) than our model, likely due to their more
253 complex ANN configuration (two hidden layers with 128 nodes each) and the including of sample location and time into input
254 features. However, the more complex model will significantly increase the computational cost, and the incorporation of
255 location and time information may weaken the physical interpretability. On the other hand, the performance improvement is
256 very limited. Therefore, we keep the simpler model configuration.

257 The performance of the model was evaluated across each of the nine oceanic regions. As illustrated in Fig. 4c, the \log_{10} space
258 RMSEs are all below 0.33 (equivalent to a concentration ratio of 2.13 in linear space), except for the Coastal region ($RMSE =$
259 0.362 and $R^2 = 0.384$). Since the Coastal region comprises only 9.7% of the global oceanic area, the comparatively lower
260 performance in this area has minimal impact on the overall ability to predict the spatiotemporal distributions of DMS on a
261 global scale. Despite the R^2 values in Trades_Pacific and Trades_Atlantic being lower than 0.5, which is related to the relatively
262 narrow variation range of DMS concentration, the RMSEs in these regions remain quite low and comparable to those of other
263 regions. In general, our ANN ensemble model demonstrates a satisfactory capacity to reproduce variations in DMS
264 concentrations across diverse oceanic regions.

265 While we have implemented a weighted resampling strategy to bolster the number of samples with extreme DMS
266 concentrations prior to training, aiming to enhance the model performance in predicting such extreme values, the model still
267 tends to underestimate the extremely high DMS concentrations and overestimate the extremely low concentrations (Fig. 4 and
268 Fig. S4). Consequently, significant positive correlations emerge between prediction residuals (observation – prediction) and
269 observed $\log_{10}(\text{DMS})$, particularly evident in Coastal and Trades regions, where the slopes exceed 0.55 (Fig. 5 and Fig. S6).
270 Given the scarcity of observational data in these high-DMS and low-DMS regimes, it is considerable challenge to completely
271 address this issue without succumbing to overfitting via purely data-driven approaches. The data augmentation by weighted
272 resampling can only partially alleviate this issue. It underscores imperative for acquiring more observational data on sea surface
273 DMS in future endeavours. Moreover, integrating DMS biogeochemical mechanisms with machine learning techniques may
274 offer a promising avenue to tackle this challenge.

275 Owing to the underestimation of high DMS concentrations, a negative mean bias (MB) in DMS concentration is evident across
276 all regions, ranging from -0.23 to -1.48 nM (Table 2). The normalized mean bias (NMB, the ratio between mean bias and mean
277 observed concentration) ranges from -11.1% to -32.1%. The most significant NMB emerges in Coastal and Trades_India
278 regions, while NMB remains within -20% for other regions. The global MB and NMB are -0.77 nM and -16.2%, respectively.
279 It is worth noting that these biases are compared against historical DMS observations, which were conducted within a very
280 limited geographical area and time periods. Thus, they cannot be interpreted as the actual mean modelling bias for the entire
281 region. On the other hand, these extreme DMS concentrations represent only a minority of the entire sample set. Our model
282 adeptly reproduces the majority of observations with moderate DMS concentrations across all regions, with the percentage of
283 simulated values falling within 1/3 to 3 times of observations ranging from 88.0% to 99.3%.

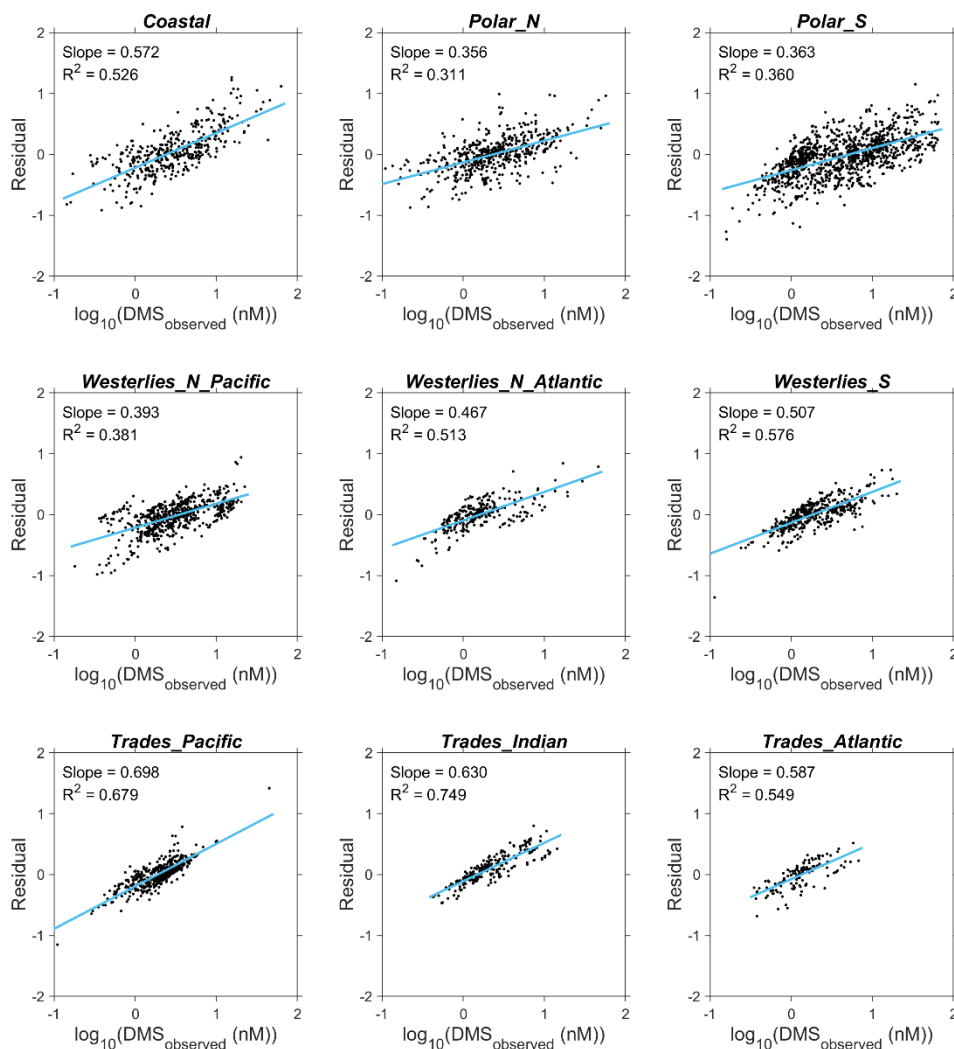
284



285

286 **Figure 4.** Comparisons between ANN-simulated and observed DMS concentrations. (a) Scatter density for simulated versus
 287 observed DMS concentrations of the samples used in ANN training. This plot corresponds to the original data before

288 resampling and only a subset of coastal data are included to maintain F_{coastal} at 9.7%, which aligns with data composition in
 289 training. (b) Comparison between the simulated versus observed DMS concentrations of testing set. (c) Comparison between
 290 the simulated versus observed DMS concentrations of testing set across 9 regions. The number of data points (n), the \log_{10}
 291 space R^2 and the root mean square error (RMSE) are also displayed.
 292



293
 294 **Figure 5.** Correlations between prediction residuals of $\log_{10}(\text{DMS})$ and observed values across different regions
 295 corresponding to the testing set.

296
 297 **Table 2.** The mean bias and normalized mean bias of the ANN-predicted DMS concentrations against observations across
 298 different regions.

Region	Mean bias (nM)	Normalized mean bias
Coastal	-1.48	-29.6%
Polar_N	-0.62	-14.9%
Polar_S	-1.09	-13.0%
Westerlies_N_Pacific	-0.74	-15.3%
Westerlies_N_Atlantic	-0.25	-11.1%
Westerlies_S	-0.44	-17.1%
Trades_Pacific	-0.23	-10.3%
Trades_Indian	-0.88	-32.1%
Trades_Atlantic	-0.24	-13.6%
Global	-0.77	-16.2%

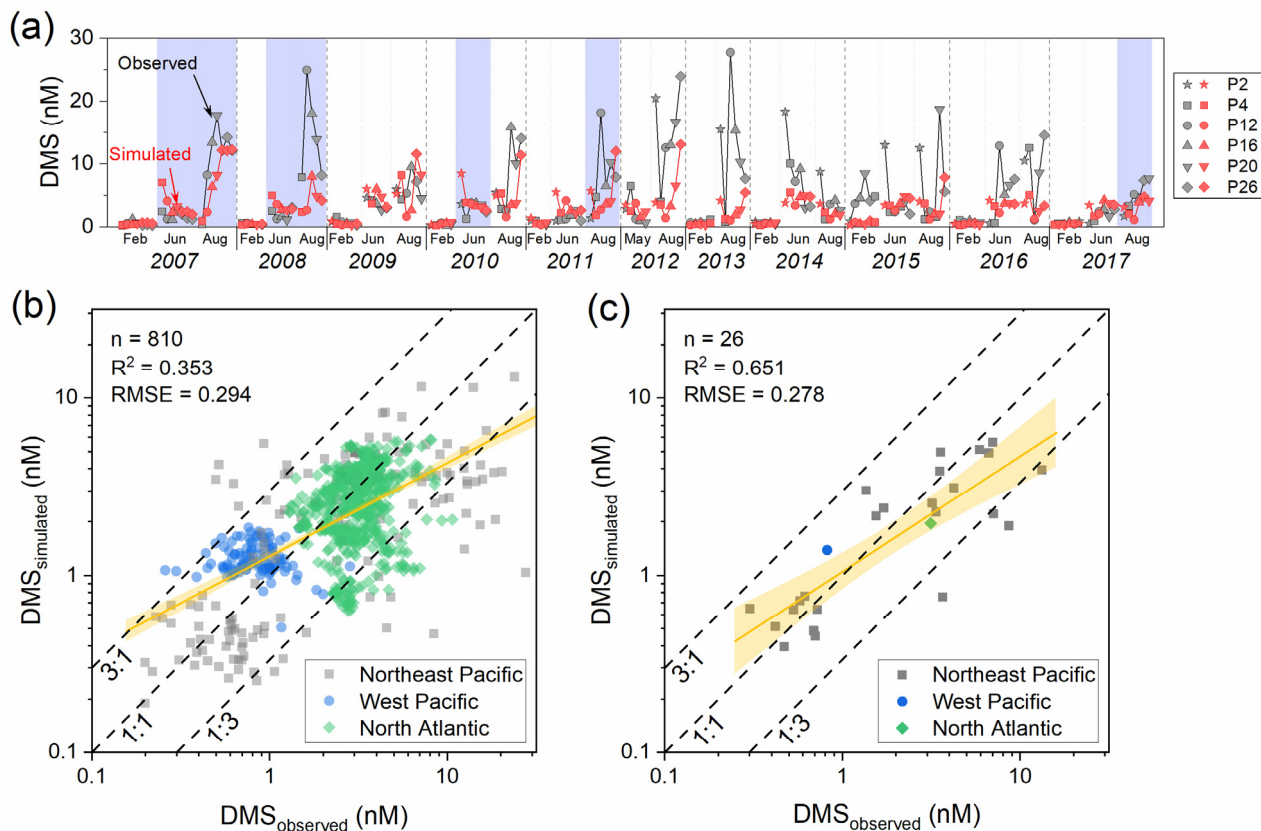
299

300

301 It is worth noting that there may be intrinsic connections between the 10% excluded testing subset and the training set, because
302 the data from the same cruise or fixed-site campaign have certain continuity. To further evaluate the reliability of the ANN
303 model, we compared the simulated DMS concentrations with the observational data from fully independent campaigns, which
304 are obtained from 33 cruises in Northeast Pacific, West Pacific, and North Atlantic (number of data = 6,478). These data
305 include (1) discrete sampling and measurement during 31 cruises of *Line P Program* in Northeast Pacific (Steiner et al., 2011)
306 (9 February 2007 – 26 August 2017, number of data = 177, <https://www.waterproperties.ca/linep/index.php>, last access: 23
307 November 2020), (2) underway measurements during *SONNE cruise 202/2 (TRANSBROM)* in West Pacific (Zindler et al.,
308 2013) (9 – 23 October 2009, number of data = 115, <https://doi.org/10.1594/PANGAEA.805613>, last access: 23 November
309 2020), (3) underway measurements during the third *North Atlantic Aerosols and Marine Ecosystems Study (NAAMES)*
310 campaign (Behrenfeld et al., 2019; Bell et al., 2021) (6 – 24 September 2017, number of data = 1,025,
311 <https://seabass.gsfc.nasa.gov/naames>, last access: 27 November, 2020). Before the comparison, the data measured within a
312 $0.05^{\circ} \times 0.05^{\circ}$ grid and at the same day were binned by arithmetic average.

313 The comparisons between these observed DMS concentrations and ANN simulation are shown in Fig. 6. Regarding the *Line*
314 *P Program*, it should be noted that there are 7 cruises included in the GSSD database, but those data were obtained by underway
315 measurements, different from the discrete sampling (Niskin bottle) data used here. Hence, these cruises were retained and
316 marked in Fig. 6a but excluded in subsequent statistical analysis (Fig. 6b-c). It can be seen that the model effectively captures
317 the seasonal variation in Northeast Pacific, which is generally August > June > February (Fig. 6a). However, the small-scale
318 spatial variations can only be partially reproduced by the model in certain campaigns, such as those in June and August of
319 2007, June of 2009, August of 2012, and August of 2016. Notably, the model generally underestimates high DMS
320 concentrations during summer, particularly those exceeding 10 nM, consistent with earlier discussions. Aggregating data from
321 all campaigns across three regions, the \log_{10} space RMSE of simulated DMS concentrations against observations is 0.294,

322 marginally higher than the training set. Most simulated values (87.8%) are within the range of 1/3 to 3 times of observations.
 323 The results further evidence that there is no significant overfitting in our model. When data from each campaign are binned,
 324 simulations demonstrate high consistency with observations, as depicted in Fig. 6c (RMSE = 0.278, $R^2 = 0.651$). In summary,
 325 although our ANN ensemble model may not precisely reproduce small-scale variations and extreme values in specific regions
 326 and periods, it reasonably captures overall large-scale variations.
 327



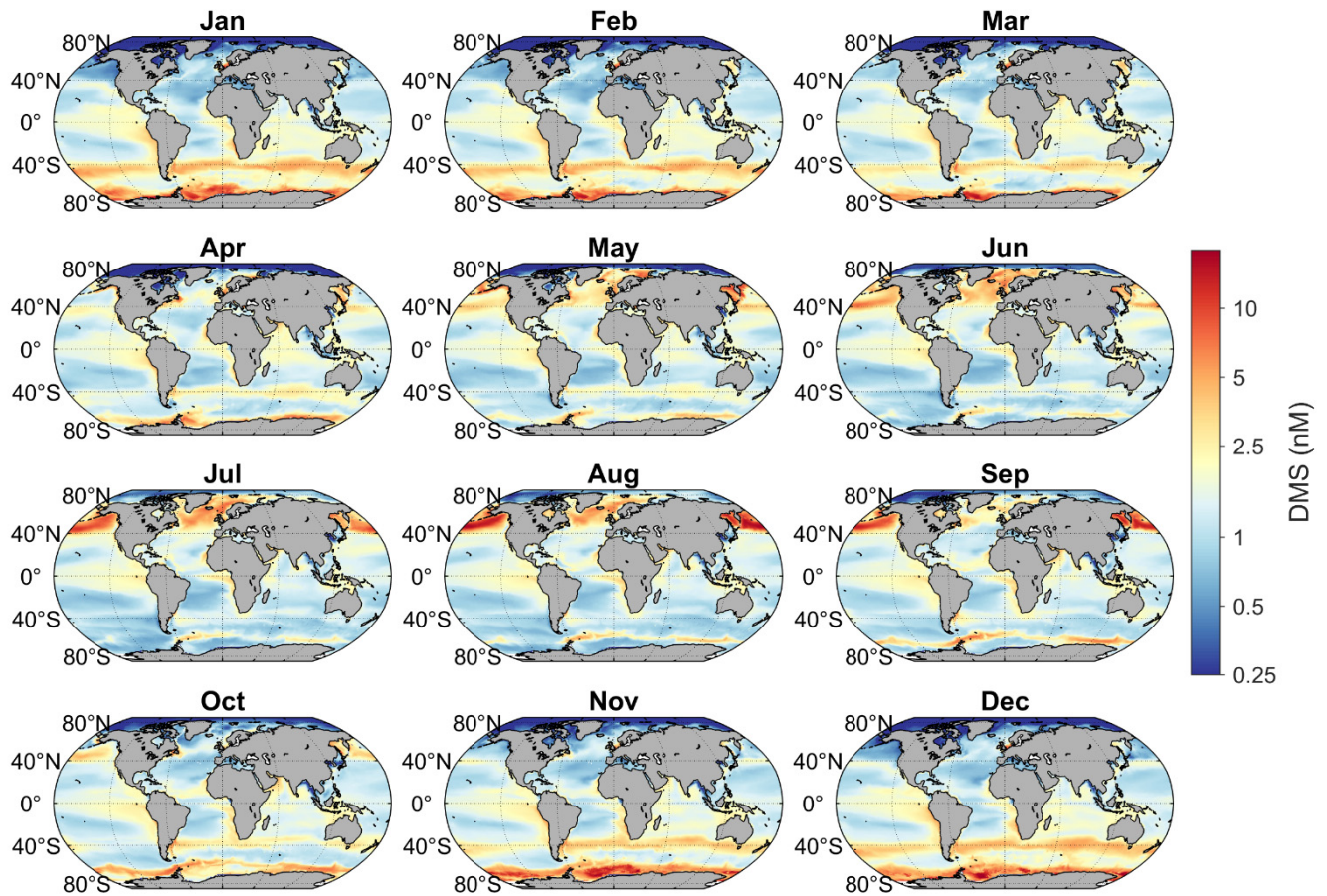
328
 329 **Figure 6.** Comparisons between the ANN predictions and observations from fully independent campaigns. (a) Time series of
 330 simulation results and DMS observational data obtained from *Line P Program*. The different markers represent different
 331 stations of *Line P*. The blue shades cover the data obtained from the cruises included in the GSSD database but with a different
 332 method. (b) Scatter plot of simulated versus observed DMS concentrations. (c) The same as panel b but for averaged data of
 333 each cruise. The yellow lines and shaded bands are linear fittings and corresponding 95% confidence intervals for \log_{10} space
 334 data. The R^2 and RMSE displayed in the figure also correspond to \log_{10} space data.

335 3.2 DMS distribution

336 3.2.1 Spatial and seasonal variations

337 The monthly climatology of ANN-simulated DMS concentrations in the global sea surface from 1998 to 2017 is shown in Fig.
338 7. Overall, the DMS concentrations in mid- and high-latitude regions exhibit a significant seasonal cycle, peaking in summer
339 and reaching their lowest in winter. This pattern aligns with the results of many prior observational studies. In the northern
340 hemisphere, elevated DMS concentrations (>2.5 nM) during summer mainly occur in two regions. One is the North Pacific
341 (40° – 60° N) where the concentration generally peaks in August, surpassing 10 nM (Fig. 7). The other is the subarctic North
342 Atlantic (45° – 80° N). A notable increase of DMS concentration starts around 45° – 50° N in May and gradually shifts northward
343 beyond 50° N by July (Fig. 7-8). This spatiotemporal evolution pattern corresponds to the evolution of solar radiation intensity
344 and the spring-summer bloom patterns of phytoplankton (Friedland et al., 2018; Yang et al., 2020). The peak concentration
345 date at the same latitude in the North Atlantic generally precedes that in the North Pacific (Fig. 8). In the southern hemisphere,
346 there is a conspicuous DMS-rich zone near 40° S (where the Subtropical Convergence lies) in summer, delineating a ring-
347 shaped high-concentration band nearly parallel to the latitude. The highest seasonal mean concentration (December–February)
348 occurs at 42.5° S, reaching 4.02 nM (Fig. 10). Southward from this zone, a low-DMS area spans 49° – 59° S, where the average
349 concentration is below 2.5 nM across all seasons. However, in the coastal waters of Antarctica (south of 60° S), significantly
350 high concentrations also manifest in summer, surpassing 5.0 nM, even higher than those near 40° S (Fig. 7 and 10). In addition
351 to the above regions, several typical upwelling zones also exhibit relatively higher DMS concentrations, such as the eastern
352 Pacific and the Southeast Atlantic. The former, situated at lower latitudes, shows no distinct seasonal variation, while the latter
353 exhibits higher concentrations from October to February. The high nutrient concentrations in upwelling areas can bolster
354 primary productivity, intensifying biological activities and augmenting the production of biogenic sulfur.

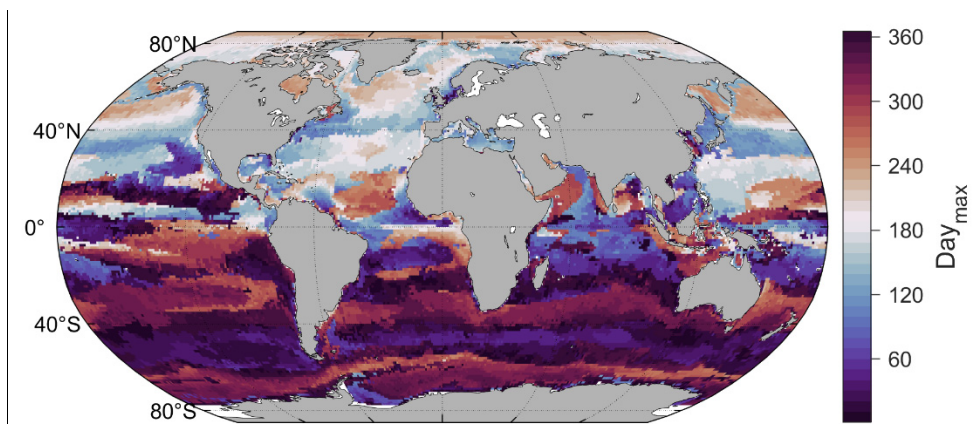
355



357

358 **Figure 7.** Monthly climatology of global sea surface DMS concentration during 1998 to 2017.

359



360

361 **Figure 8.** The day of the year with the highest sea surface DMS concentration for each grid point.

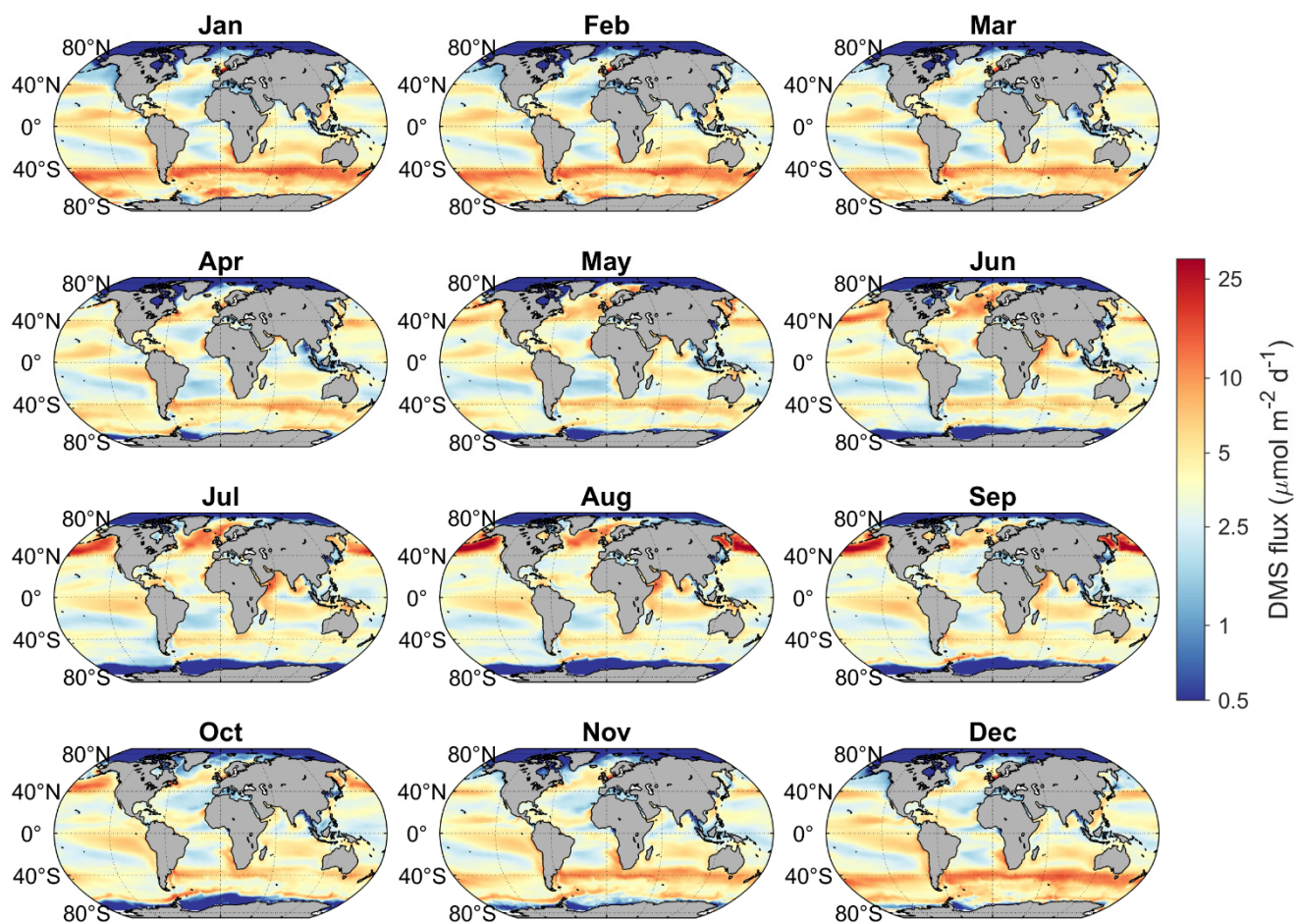
362

363 The spatiotemporal variation of DMS emission flux is generally consistent with that of concentration. As shown in Fig. 9,
364 DMS fluxes are also significantly higher in summer across most mid- and high-latitude regions, and the high-flux regions
365 generally overlap with the hot spots of DMS concentration. This indicates that the distribution of sea surface DMS
366 concentration is the main factor controlling the monthly variation pattern of DMS emissions at the global scale, and the effect
367 of transfer velocity is secondary. However, certain regions present inconsistencies between DMS flux and concentration
368 dynamics. For instance, in the Arabian Sea and the central Indian Ocean, elevated transfer velocities (Fig. S7) during the June
369 to September, driven by heightened wind speeds, markedly enhance emission fluxes, despite comparatively lower
370 concentrations than other months. In polar regions, especially along the coast of Antarctica, although the DMS concentration
371 is high in summer, sea ice coverage significantly impedes DMS release, thus the emission flux remains at a low level.

372 As shown in Fig. 10, the higher wind speeds in autumn and winter at mid- and high-latitudes result in higher total transfer
373 velocities, leading to smaller summer-to-winter ratios of DMS emission flux compared to that of DMS concentration. In low
374 latitudes, the existence of the trade wind zones in both hemispheres further leads to two high-flux bands between 5° to 20°.
375 The emission fluxes in the equatorial region between these two trade zones are significantly lower. Although the latitudinal
376 distributions of mean DMS emission fluxes in the southern and northern hemispheres are almost symmetrical, the huge
377 difference in ocean area between the two hemispheres results in a significantly higher total emission from the southern
378 hemisphere. Since anthropogenic SO₂ emissions are mainly concentrated in the northern hemisphere, oceanic DMS plays a
379 much more important role in the southern hemisphere, especially over the regions south of 40° S where the DMS emission is
380 high and the perturbation of anthropogenic pollution is low.

381 According to our newly built DMS gridded dataset, the global area-weighted annual mean concentration of DMS at the sea
382 surface from 1998 to 2017 was ~1.72 nM (1.67–1.76 nM), which is within the range among the values (1.6 to 2.4 nM) obtained
383 by various methods in previous studies (Tesdal et al., 2016). The global annual mean DMS emission to the atmosphere was
384 17.0 TgS yr⁻¹ (16.6–17.4 TgS yr⁻¹), with 10.3 TgS yr⁻¹ (60.6%) from the southern hemisphere and 6.7 TgS yr⁻¹ (39.4%) from
385 the northern hemisphere.

386

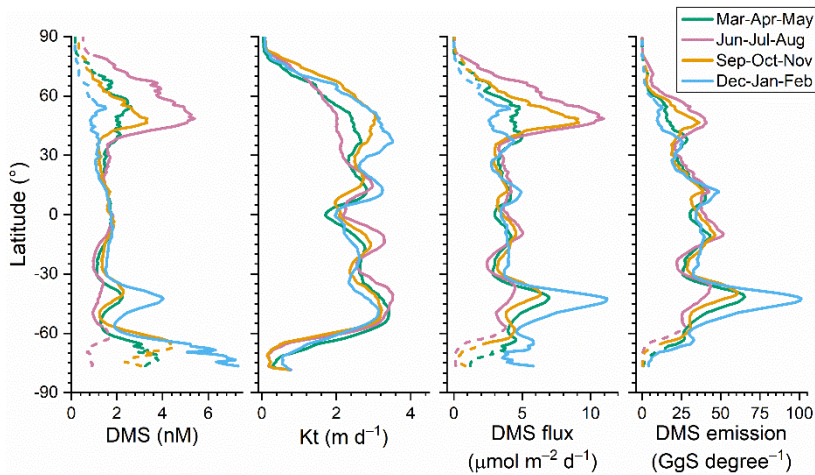


388

389 **Figure 9.** Monthly climatology of global DMS sea-to-air flux from 1998 to 2017.

390

391



392

393 **Figure 10.** Latitudinal distributions of sea surface DMS concentration, total transfer velocity (Kt), sea-to-air flux, and total
 394 emission in different seasons during 1998–2017. The dashed parts of the lines represent the missing ratio of satellite Chl *a* data
 395 for DMS simulation is higher than 0.5, thus most Chl *a* data is from CMEMS global biogeochemical multi-year hindcast.

396

397 3.2.2 Comparisons with other global DMS climatologies

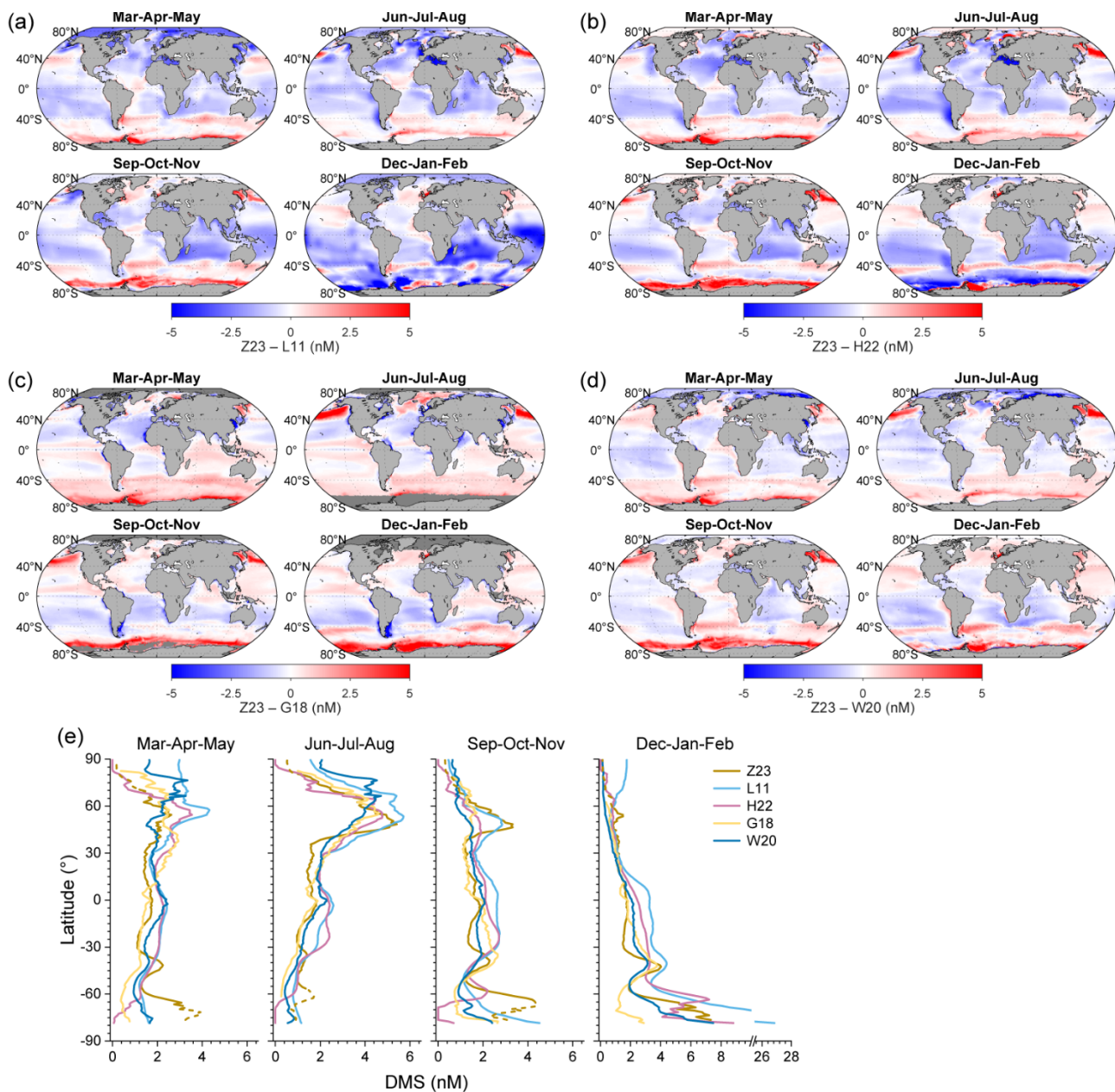
398 Here we compare the distributions of DMS concentration derived from our ANN simulation (referred to as Z23) with four
 399 previously constructed climatologies (Fig. 11), including (1) L11: the widely used second version of
 400 interpolation/extrapolation-based climatology established by Lana et al. (2011), (2) H22: an updated version of L11
 401 incorporating much more DMS measurements and using dynamic biogeochemical provinces (Hulswar et al., 2022), (3) G18:
 402 the DMS concentration field estimated by a two-step remote sensing algorithm (Galí et al., 2018), and (4) W20: the previous
 403 DMS climatology simulated by ANN (Wang et al., 2020).

404 Overall, all datasets exhibit the general pattern of high DMS concentration during summer and low concentration during winter,
 405 but notable distinctions emerge in their specific distributions. Due to the limitation of the method used, DMS_{L11} exhibits
 406 relatively lower spatial heterogeneity (i.e., higher patchiness), which may not well capture the detailed spatial variability on a
 407 regional scale. Compared with DMS_{L11}, DMS_{Z23} is significantly lower at high latitudes during summer and in the South Indian
 408 Ocean and Southwest Pacific Ocean from December to February (Fig. 11a). Particularly in the southern polar region (Polar_S),
 409 latitudinal averages of DMS_{L11} surpass 10 nM during summer, which are 1–3 times higher than DMS_{Z23} (Fig. 11e). However,
 410 DMS_{Z23} maintains a similar level around the Antarctic in March compared to summer, and it is significantly higher than
 411 DMS_{L11} as well as other three climatologies. DMS_{H22} shows lower disparities with DMS_{Z23} in the Arctic, the South Indian
 412 Ocean, and the Southwest Pacific Ocean, but the summertime concentrations in most of Polar_S region are also > 2 nM higher
 413 than DMS_{Z23} (Fig. 11b). In contrast, DMS_{H22} in Polar_S from September to November is > 2 nM lower than DMS_{Z23}. The

414 global area-weighted annual mean DMS concentrations in L11 and H22 are 2.43 nM and 2.26 nM, respectively, which are
415 approximately 41.3% and 31.4% higher than Z23.

416 G18 exhibits the lowest global annual mean concentration (1.63 nM) among these climatologies, approximately 5.2% lower
417 than Z23. The most notable deviation occurs in the North Pacific during boreal summer and near the Antarctic during austral
418 summer and autumn, where DMS_{Z23} is > 5 nM ($> 100\%$) higher than DMS_{G18} (Fig. 11c). Conversely, there are high DMS
419 concentrations (> 5 nM) in certain coastal seas (such as the coasts of East and Northeast Asia, the coasts of Patagonia and Peru,
420 the southwestern coast of Africa, and the western coasts of North America and the Sahara Desert) based on the G18 estimate.
421 This characteristic is not fully replicated by other DMS fields, possibly due to the overestimation of Chl *a* by satellites in
422 coastal regions caused by the interference of colored dissolved organic matters and non-algal detrital particles (Aurin and
423 Dierssen, 2012). W20 exhibits the highest consistency with Z23 in spatiotemporal distribution patterns as well as the lowest
424 difference in global annual mean concentration (1.74 nM, only 1.2% higher than Z23). However, notable discrepancies exist
425 in specific regions. For instance, during summertime, DMS_{Z23} is > 1 nM ($> 40\%$) lower than DMS_{W20} in more than half of the
426 Arctic area, while in North Pacific and Southern Ocean DMS_{Z23} is significantly higher than DMS_{W20} (Fig. 11d). Furthermore,
427 only DMS_{Z23} forms a nearly complete high-concentration annular band at $\sim 40^\circ$ S during austral summer.

428



429

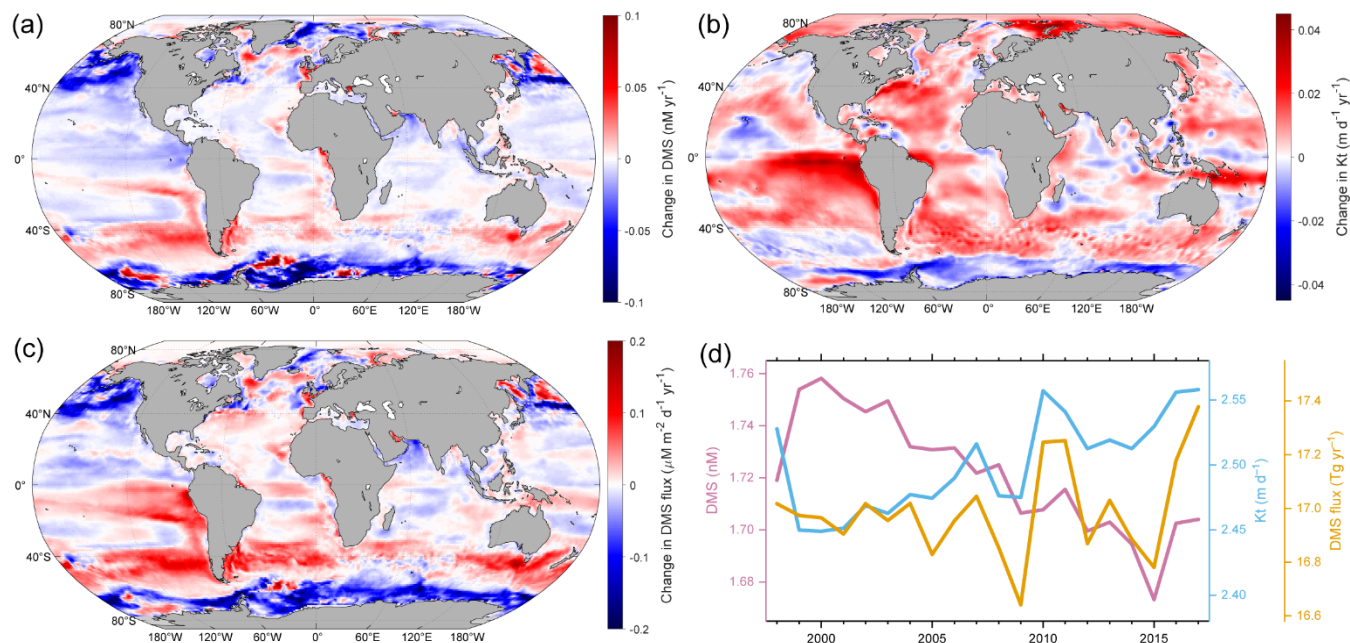
430 **Figure 11.** (a–d) The spatial distributions of DMS concentration differences between Z23 and four previously estimated fields
 431 across different seasons: (a) L11, (b) H22, (c) G18, and (d) W20. Dark gray regions in the ocean represent data missing in at
 432 least one field. (e) Comparisons between the latitudinal distributions of Z23 and four previous DMS fields across different
 433 seasons. The dashed parts of the Z23 lines represent the missing ratio of satellite Chl *a* data for DMS simulation is higher than
 434 0.5, thus most Chl *a* data is from CMEMS global biogeochemical multi-year hindcast.

435

436 3.2.3 Decadal changes

437 One of the advantages of our ANN-derived DMS dataset is its time-resolved nature, which enables us to investigate the
438 interannual variations in sea surface DMS concentration and flux. Here we present the decadal trends of DMS concentration,
439 Kt, and emission flux spanning from 1998 to 2017 at both global and regional scales. Overall, the absolute interannual
440 variability of DMS concentration across most global oceanic regions appears relatively small. 85.3% of the global oceanic
441 area exhibited a difference of less than 1 nM between the maximum and minimum annual average concentrations during this
442 20-year period, particularly evident in tropical and subtropical regions with latitudes between 40° S and 40° N. At latitudes
443 higher than 40° in both hemispheres, notable decadal changes occurred (Fig. 12a). Annual mean DMS concentrations in the
444 Greenland Sea, the North Pacific, and the Southern Ocean exhibited significant decreasing trends with rates exceeding 0.03
445 nM yr⁻¹ ($P < 0.05$). A significant decreasing trend was also noted in the eastern tropical Pacific Ocean, albeit at a much lower
446 absolute rate, primarily below 0.015 nM yr⁻¹. Conversely, there were significant increasing trends in the Labrador Sea, the
447 South Pacific (35° S – 60° S, 150° E – 75° W), and the southeastern Pacific, with the highest rate exceeding 0.02 nM yr⁻¹. The
448 global annual mean concentration exhibited a decreasing trend with a rate of 0.0033 nM yr⁻¹ ($P < 0.05$, Fig. 11d). The highest
449 value (1.76 nM) occurred in 2000, and the lowest concentration (1.67 nM) occurred in 2015. Due to the primary influences of
450 increasing WS and secondary impact of rising SST in most mid- and low-latitude regions (Fig. S8), the Kt of DMS also showed
451 an overall increasing trend, especially in the eastern Pacific and Atlantic Ocean (Fig. 12b). The increase in Kt can offset the
452 decrease in DMS concentration to some extent, resulting in no significant trend in global DMS emissions during this 20-year
453 period (Fig. 12d).

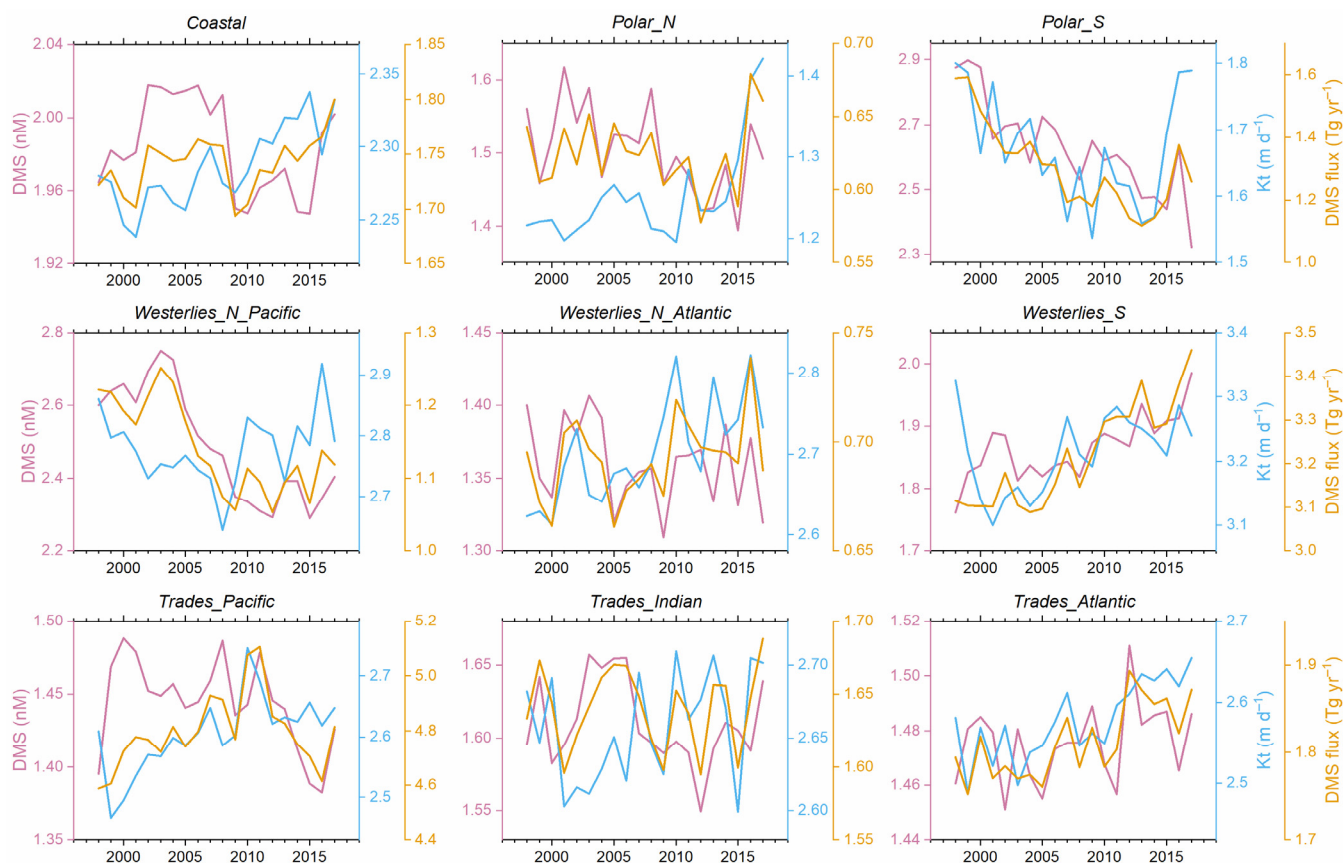
454 In the Arctic region, which stands as one of the most sensitive areas to climate warming (Screen et al., 2012; Serreze and Barry,
455 2011), the sea ice coverage has undergone significant reduction over the past 2 decades, particularly noticeable in the Barents
456 Sea and Kara Sea, and further north ($> 1\% \text{ yr}^{-1}$ for annual mean SI, Fig. S8). The retreat of summertime sea ice leads to an
457 expansion of open-sea surface, potentially amplifying DMS emission (Galí et al., 2019). However, despite this trend, there
458 was no significant increase in the annual total emission from the Polar_N region over the same period, primarily due to a
459 decreasing trend in DMS concentration (Fig. 13). On the other hand, the highest emission took place in the last two years ($>$
460 0.65 Tg yr⁻¹), attributed to the highest Kt. Thus, it is likely that a rise in DMS emission will appear in future Arctic region with
461 further loss of sea ice coverage (Galí et al., 2019). In contrast to the Arctic, the Southern Ocean has experienced a significant
462 increase in sea ice fraction (Fig. S8), leading to a significant decrease in Kt (Fig. 12b). Coupled with the decreased DMS
463 concentration, it resulted in a substantial decline in the DMS emission flux (Fig. 12c and 13). The highest annual total emission
464 flux in the Polar_S region occurred in 1998 (1.42 TgS), while the lowest occurred in 2013 (1.12 TgS), representing a decrease
465 of ~21%. Across other oceanic regions, the annual average DMS concentrations in the Westerlies_N_Pacific and
466 Trades_Pacific regions exhibit decreasing trends over the past 20 years, while the concentration in Westerlies_S has increased
467 ($P < 0.05$, Fig. 13). Regarding DMS flux, the Westerlies_N_Pacific showed a decrease, while the Westerlies_S and
468 Trades_Atlantic showed an increase. There was no significant trend in other low- and mid-latitude regions.



470

471 **Figure 12.** (a–c) The spatial distributions of changes in (a) DMS concentration, (b) Kt, and (c) DMS emission flux from 1998
 472 to 2017. The linear regression slopes for the annual means are taken as the changing rates here. (d) The temporal changes of
 473 global annual mean DMS concentration, Kt, and total emission flux from 1998 to 2017.

474



476

477 **Figure 13.** The temporal changes of annual mean DMS concentration, Kt, and total emission flux in different regions from
 478 1998 to 2017.

479 3.3 Connection with atmospheric biogenic sulfur

480 One of the primary objectives of developing this daily gridded DMS dataset (Z23) spanning multiple years is to improve the
 481 emission inventory of marine biogenic DMS, thereby enhancing the modelling performance for atmospheric sulfur chemistry,
 482 especially for simulating sulfur-containing aerosols. To assess whether our newly constructed DMS dataset can reach this
 483 objective, we employed a backward trajectory-based method to examine the correlation between sea surface DMS emissions
 484 and resulting DMS oxidation products in the atmosphere. The correlation was then compared against those derived from
 485 previously reported DMS climatologies (L11, H22, G18, and W20).

486 Here we use the observed concentrations of particulate methanesulfonic acid (MSA) over the Atlantic Ocean as a reference.
 487 MSA is one of the major end-products of DMS in the atmosphere and is solely from the oxidation of marine biogenic DMS

488 over remote oceans (Saltzman et al., 1983; Savoie et al., 2002; Osman et al., 2019). Therefore, there is likely to be a dependence
489 of the variation of MSA concentration on the DMS emission fluxes. During four transection cruises in the Atlantic conducted
490 by *R/V Polarstern* (20 April – 20 May 2011, 28 October – 1 December 2011, 10 April – 15 May 2012, and 27 October – 27
491 November 2012), the MSA concentrations in submicron aerosols were measured online using a High-Resolution Time-of-
492 Flight Aerosol Mass Spectrometer. The ship tracks are shown in Fig. S9, and detailed information about the cruises and
493 measurement methodology was provided by Huang et al. (2016). The 72-hour air mass backward trajectories reaching the ship
494 position were calculated every hour by the HYSPLIT model, starting from a height of 100 m (Stein et al., 2015). Subsequently,
495 the air mass exposure to DMS emission (AEDMS), denoting the weighted average of DMS emission flux along the trajectory
496 path, was calculated following the approach of Zhou et al. (2021). We used 5 different DMS gridded datasets, including Z23,
497 L11, H22, G18, and W20. For Z23, the calculated daily DMS fluxes were utilized. For the remaining 4 monthly climatologies,
498 we applied the daily Kt data from Z23 to calculate the DMS fluxes, thus eliminating the potential confounding influences
499 stemming from different Kt parameterizations. In this calculation, the same concentration was assigned to all days within a
500 month without interpolation. Detailed procedures for the calculation of AEDMS are elucidated in Appendix C.

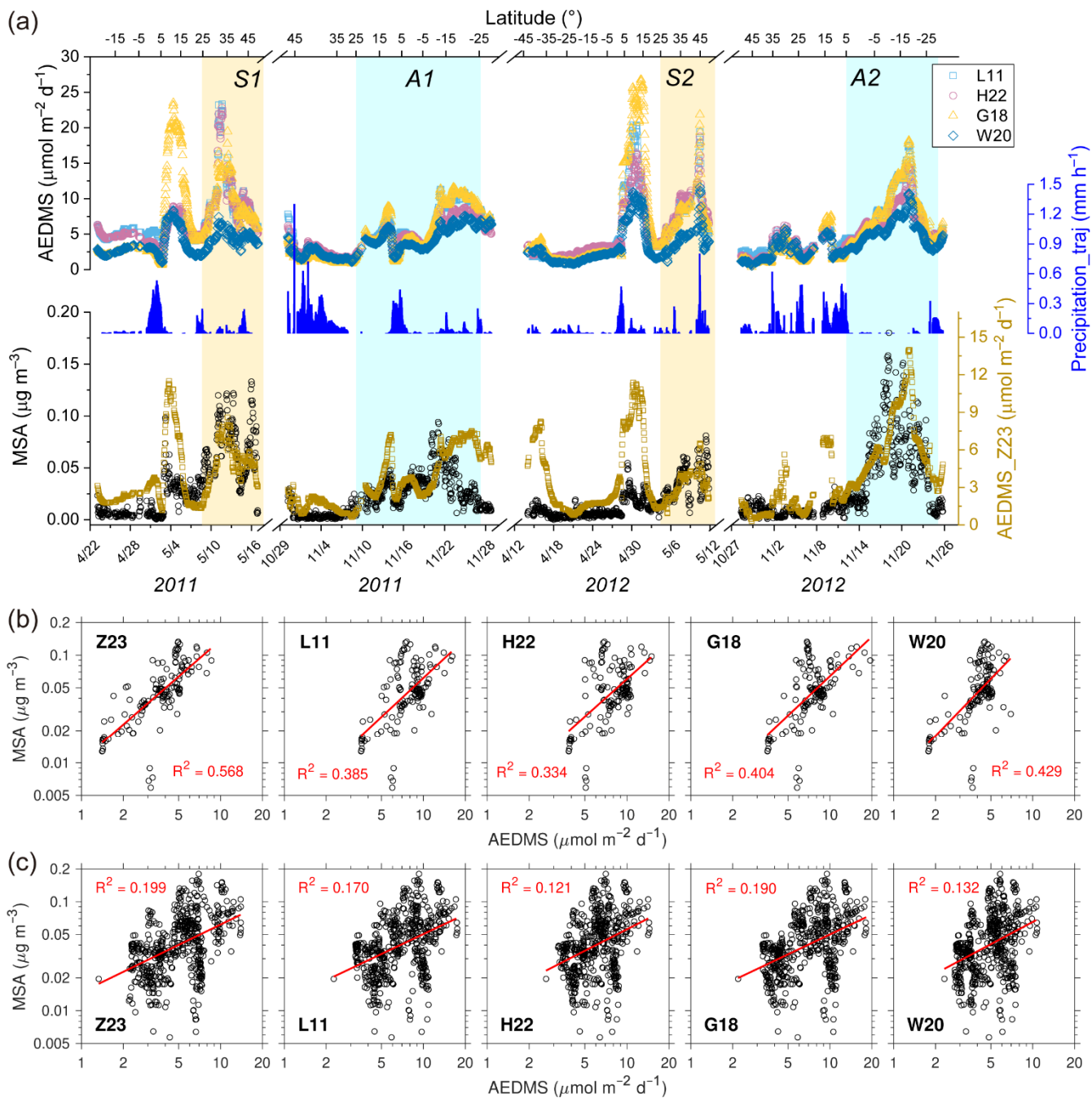
501 MSA concentrations were significantly higher in late spring than those in autumn for both North and South Atlantic Oceans
502 (Fig. 14a). For example, during the boreal spring cruise in 2011, the average MSA concentration over the North Atlantic (0.068
503 $\mu\text{g m}^{-3}$, north of 25°N) was about an order of magnitude higher than the average concentration over the South Atlantic (0.006
504 $\mu\text{g m}^{-3}$, south of 5°S). During the boreal autumn cruise in 2011, the average concentration over the South Atlantic (0.034 μg
505 m^{-3} , south of 5°S) was ~ 5 times higher than that over the North Atlantic (0.006 $\mu\text{g m}^{-3}$, north of 25°N). In addition to this
506 major seasonal pattern, there was also a minor MSA concentration peak between 5° – 15°N in both seasons. The spatial and
507 seasonal variations of AEDMS based on the Z23 dataset (referred to as AEDMS_Z23) largely coincided with these MSA
508 concentration patterns (Fig. 14a). It should be noted that the MSA/AEDMS ratio between 5° – 15°N was significantly lower
509 than those in other high-MSA regions, which may result from the DMS simulation biases near the coast of West Africa or the
510 lower DMS-to-MSA conversion yields related with air temperature and oxidant species (Barnes et al., 2006; Bates et al., 1992).
511 There were also several AEDMS peaks in North Atlantic during November 2012, inconsistent with the continuously low MSA
512 concentrations. Given the high precipitation rates along the trajectory (Fig. 14a), a strong wet scavenging process might
513 significantly reduce aerosol concentrations (Wood et al., 2017).

514 The AEDMS derived from other DMS concentration fields showed similar variations to AEDMS_Z23 (Fig. 14a). It is not
515 surprising since all DMS concentration fields exhibit similar large-scale spatiotemporal patterns, and identical air mass
516 transport path and Kt were applied in different AEDMS calculations. However, due to the lower temporal resolutions and
517 absence of interannual changes in those DMS monthly climatologies, the resulting AEDMS may be less effective in capturing
518 variability at finer scales or across different years. Here we focus on the high-MSA periods to elaborate on this issue, which
519 corresponds to latitudes north of 25°N in boreal spring (S1 and S2 in Fig. 14a), 25°N – 25°S in boreal autumn of 2011 (A1

520 in Fig. 14a), and south of 5° N in boreal autumn of 2012 (A2 in Fig. 14a). As shown in Fig. 14b, hourly MSA concentrations
521 exhibited significantly stronger correlations with AEDMS_Z23 than with other AEDMS time series in S1 and S2, indicating
522 AEDMS_Z23 can explain more (1.32 – 1.70 times) variance of MSA concentration. During A1 and A2, the correlations
523 between AEDMS and MSA concentration were weaker than those during S1 and S2, possibly due to higher DMS prediction
524 biases in South Atlantic or different influencing factors on atmospheric DMS chemistry across wide spatial ranges. Nonetheless,
525 AEDMS_Z23 still exhibited the highest correlation with MSA (Fig. 14c). This overall stronger connection between Z23 and
526 atmospheric DMS-derived aerosols mainly benefited from the combined effects of higher time resolution and inherent
527 interannual variations. For example, the ratio of average MSA concentration during S1 to that during S2 (S1-to-S2 ratio) was
528 1.89, and the A2-to-A1 ratio was 1.75. AEDMS_Z23 exhibited a slightly lower but still significant interannual variation degree,
529 where the S1-to-S2 ratio and A2-to-A1 ratio were 1.60 and 1.45, respectively. However, this interannual variation cannot be
530 reproduced by other datasets, where the S1-to-S2 ratio and A2-to-A1 ratio were in the range of 1.08–1.30 and 1.19–1.29,
531 respectively. These results manifest the potential of our newly developed DMS gridded data product to enhance the modeling
532 performance for atmospheric DMS processes compared with previously reported climatologies.

533 It is worth noting that the satellite-based algorithms of G18 and ANN model of W20 can also be utilized to produce daily
534 multiyear DMS fields as Z23. Future investigations could include comparisons with these fields, facilitating a more
535 comprehensive assessment of the performance of each algorithm/model. Furthermore, the AEDMS method used here is a
536 highly simplified approach without considering the complex DMS chemistry in the atmosphere, and the intercomparisons
537 based on chemical transport models can be used in the future to obtain a more straightforward conclusion.

538



539

540 **Figure 14.** (a) Time series of observed MSA concentration, AEDMS calculated based on different DMS concentration datasets,
 541 and average precipitation along the backward trajectory (Precipitation_traj) during four Atlantic cruises in 2011–2012. (b–c)
 542 Correlations between hourly MSA concentration and AEDMS based on different DMS concentration datasets (b) during

543 periods S1 + S2 and (c) during periods A1 + A2. Data points during the periods with air mass time fraction within the boundary
544 layer less than 90% or Precipitation_traj larger than 0.05 mm h⁻¹ were removed.

545 **4 Uncertainties and limitations**

546 Although our ANN ensemble model and derived DMS dataset demonstrate certain advantages compared to previous studies,
547 as discussed in Section 3.3, there persist notable uncertainties and limitations, which result in the ~39% uncaptured variance
548 (Fig. 4a) and non-negligible simulation biases. Firstly, the data of input features from different sources and the observed sea
549 surface DMS concentrations inherently possess certain uncertainties, which can introduce biases in the ANN learning process.
550 Secondly, ANN models may not fully capture all intricate data patterns, and the outcomes from each training may exhibit
551 certain randomness. In this study, the average standard deviation of simulated log₁₀DMS values from 100 neural networks is
552 0.244, and the 5%-95% range of the coefficient of variation for DMS concentration is 0.18–2.54, with an average of 0.72. If
553 the detailed uncertainties associated with each data source are known, future investigations could employ Monte Carlo methods
554 to estimate the uncertainties of final results arising from the aforementioned two factors (Abdar et al., 2021; Moradkhani et al.,
555 2012). Thirdly, although the DMS observational data covers all major oceanic basins, certain regions such as the
556 Trades_Pacific remain underrepresented. Advances in online measurement technologies offer promising avenues for acquiring
557 more extensive and convenient observational data (Hulswar et al., 2022). In the future, more observations are imperative for
558 these underrepresented regions, facilitating model refinement and updates. Fourthly, as discussed in Section 3.1, the model
559 cannot well reproduce the extremely high and extremely low DMS concentrations, which potentially introduces notable biases,
560 particularly in flux calculations. We also need more observational data to help mitigate this issue.

561 Beyond the 9 variables incorporated in this study, other environmental parameters, such as pH (Six et al., 2013; Hopkins et al.,
562 2010) and trace metal elements (Li et al., 2021), can also influence DMS concentration. Not incorporating these factors may
563 introduce potential biases. Thus, further field measurements of trace metals are necessary to comprehend their spatiotemporal
564 distributions, which are likely to enhance the model's ability to simulate sea surface DMS concentrations. In terms of the
565 temporal resolution, our product significantly surpasses previous monthly climatologies. However, the higher temporal
566 resolution would be even more valuable if accompanied by higher spatial resolution. In this work, the spatial resolution is
567 limited by the ECCO dataset, where the largest spatial grid size is 110 km. Therefore, we are not able to achieve higher spatial
568 resolution without interpolation. Enhancing the spatial resolution of DMS fields using high-quality input datasets with finer
569 spatial resolution represents a prospective direction for future research.

570 When using our newly developed DMS dataset, there are two issues that need to be noted. Firstly, there is a significant portion
571 of missing satellite Chl *a* data during winter in polar regions. In such instances, the modeling data from CMEMS global
572 biogeochemical multi-year hindcast was used, which may introduce higher uncertainty. We have provided the flags indicating
573 the source of Chl *a* data for each grid in the dataset. Nevertheless, given the low phytoplankton biomass and extensive sea ice

574 coverage during winter, DMS emissions are typically at the lowest level of the year, thus the satellite data missing has a
575 relatively small impact on investigating the subsequent effects of DMS emission on atmospheric environment. Secondly, since
576 the ANN ensemble model exhibits limited capacity in accurately reproducing extremely high concentrations of DMS, the DMS
577 concentrations in certain nearshore areas with intensive biological activity may be greatly underestimated.

578

579 **5 Code and data availability**

580 The generated gridded datasets of DMS concentration, total transfer velocity, and flux have been deposited at
581 <https://zenodo.org/records/10906101> (Zhou et al., 2024) and can be downloaded publicly. The ANN model code and the
582 Matlab scripts for data analysis are available from <https://zenodo.org/record/10937598> (Zhou, 2024).

583 **6 Conclusion**

584 Based on the global sea surface DMS observations and associated data of 9 relevant environmental variables, an ANN
585 ensemble model was trained. The ANN model effectively captures the variability of DMS concentrations and demonstrates
586 good simulation accuracy. Leveraging this ANN model, a global sea surface DMS gridded dataset with a daily resolution
587 spanning 20 years (1998–2017) was constructed. The global annual average concentration was ~ 1.72 nM, falling within the
588 range of previous estimates, and the annual total emission was ~ 17.0 TgS yr⁻¹. High DMS concentrations and fluxes took place
589 during summer in North Pacific (40°–60° N), North Atlantic (50°–80° N), the annular band around 40° S, and the Southern
590 Ocean. With this newly developed dataset, the day-to-day changes and interannual variations can be investigated. The global
591 annual average concentration shows a mild decreasing trend (~ 0.0033 nM yr⁻¹), while the total emission remains stable. There
592 were more significant decadal changes in certain regions. Specifically, the annual DMS emission in the South Pacific and
593 North Pacific showed opposite trends.

594 To further validate the robustness and advantages of our new dataset, an air mass trajectory-based approach was applied to link
595 the DMS flux and atmospheric MSA concentration. Compared to previous monthly climatologies, the air mass exposure to
596 DMS calculated using our new dataset explains a greater amount of variance in atmospheric MSA concentration over the
597 Atlantic Ocean. Therefore, despite the presence of uncertainties and limitations, the new dataset holds the potential to serve as
598 an improved DMS emission inventory for atmospheric models and enhance the simulation of DMS-induced aerosols and their
599 associated climatic effects.

600

601 **Appendix A: Acronyms**

602 AEDMS Air mass exposure to DMS emission

603 ANN Artificial neural network

604	BLH	Boundary layer height
605	CCN	Cloud condensation nuclei
606	Chl <i>a</i>	Chlorophyll <i>a</i>
607	DMS	Dimethyl sulfide
608	DMSP	Dimethylsulfoniopropionate
609	DO	Dissolved oxygen
610	DSWF	Downward short-wave radiation flux
611	ECCO	Estimating the Circulation and Climate of the Ocean
612	GSSD database	Global Surface Seawater DMS database
613	K _t	Total transfer velocity
614	MLD	Mixed layer depth
615	MB	Mean bias
616	MSA	Methanesulfonic acid
617	MSE	Mean square error
618	NAAMES	North Atlantic Aerosols and Marine Ecosystems Study
619	NMB	Normalized mean bias
620	RMSE	Rooted mean square error
621	PDF	Probability distribution function
622	SI	Sea ice fraction
623	SST	Sea surface temperature
624	SSS	Sea surface salinity
625	WS	Wind speed

626

627 **Appendix B: Deriving the weighting factors for weighted resampling**

628 The probability distribution of initial log₁₀(DMS) values was fitting with a gamma distribution. The probability density
629 function is given below and displayed as the blue line in Fig. 3b.

$$630 \quad f(x) = \frac{1}{\Gamma(k)\theta^k} (x + 4)^{k-1} e^{-(x+4)/\theta} \quad (A1)$$

631 Here *k* and *θ* represent the shape parameter and scale parameter, in this case, 100.7 and 0.044, respectively. *x* is the log₁₀(DMS)
632 value. Since gamma distribution only takes positive values, we added 4 to the original *x* as the dependent variable for
633 distribution fitting. We then obtained a new gamma distribution function with the same mode but lower shape parameter, in
634 which *k* = 40 and *θ* = 0.112. The reciprocal of the new gamma distribution function was taken as the weighting factor.

635

636 **Appendix C: The calculation of air mass exposure to DMS emission (AEDMS)**

637 Here the AEDMS index followed the similar calculation of the air mass exposure to Chl *a* (AEC) in previous studies (Arnold
638 et al., 2010; Park et al., 2018; Zhou et al., 2021). We adopted the similar approach presented in Zhou et al. (2021) by replacing
639 the Chl *a* concentration with DMS flux, as shown in the following equation (A2):

$$640 \quad AEDMS = \frac{\sum_{i=0}^{72} DMS \text{ flux}_i \cdot e^{-\frac{t_i}{72} \cdot \frac{600}{BLH}}}{\sum_{i=0}^{72} e^{-\frac{t_i}{72}}} \quad (A2)$$

641 Here *i* represents the *i*-th trajectory point of the 72-hour backward trajectory (0-th for the receptor point). *DMS flux_i* represents
642 the mean DMS flux within a radius of 20 km at the location of *i*-th trajectory point. *DMS flux_i* is set to zero if the point locates
643 on land or the air mass pressure is below 850 hPa (usually in the free troposphere with little influence of surface emission). *t_i*
644 is the tracking time of the trajectory point (unit: hour) and $e^{-\frac{t_i}{72}}$ is the weighting factor to assign higher values for regions
645 closer to the receptor point. To better connect with the atmospheric concentrations in the marine boundary layer, the
646 normalization by boundary layer height (BLH) is added by the $\frac{600}{BLH}$ term. The BLH below 50 m is replaced by 50 m.

647 **Author contributions.**

648 SZ and YC designed the research. SZ, FW, ZX, and KY collected the data and did the data preprocessing. SZ implemented
649 the model development and performed the simulation with assistance from GY, HZ, and YZ. SH, HH, AW, and LP provided
650 the measurement data of atmospheric MSA over the Atlantic Ocean. SZ conducted the data analysis and visualization with
651 advice from YC and XG. SZ and YC wrote the manuscript with inputs from all authors.

652 **Competing interests.**

653 The authors declare that they have no conflict of interest.

654 **Acknowledgements.**

655 We greatly thank National Oceanic and Atmospheric Administration's Pacific Marine Environmental Laboratory for
656 maintaining the Global Surface Seawater DMS Database. We acknowledge Dr. Chenzhao Li for sharing the code of global
657 sensitivity analysis and Dr. Martin Johnson for sharing the code of DMS transfer velocity calculation. We also thank Dr. Rich
658 Pawlowicz for developing and sharing the M_Map toolbox for Matlab (<https://www.eoas.ubc.ca/~rich/map.html>), which was
659 used in the mapping of this study. XG was supported by the Research Center for Industries of the Future (RCIF) at Westlake
660 University and Westlake University Education Foundation.

661 **Financial support.**

662 This work is jointly supported by Natural Science Foundation of Shanghai (22ZR1403800), National Key Research and
663 Development Program of China (2016YFA0601304), and National Natural Science Foundation of China (41775145).

664

665 **References**

666 Abdar, M., Pourpanah, F., Hussain, S., Rezazadegan, D., Liu, L., Ghavamzadeh, M., Fieguth, P., Cao, X., Khosravi, A.,
667 Acharya, U. R., Makarenkov, V., and Nahavandi, S.: A review of uncertainty quantification in deep learning: Techniques,
668 applications and challenges, *Information Fusion*, 76, 243-297, 10.1016/j.inffus.2021.05.008, 2021.

669 Alcolombri, U., Ben-Dor, S., Feldmesser, E., Levin, Y., Tawfik, D. S., and Vardi, A.: Identification of the algal dimethyl
670 sulfide-releasing enzyme: a missing link in the marine sulfur cycle, *Science*, 348, 1466-1469, 2015.

671 Andreae, M. O.: Ocean-Atmosphere Interactions in the Global Biogeochemical Sulfur Cycle, *Mar. Chem.*, 30, 1-29, Doi
672 10.1016/0304-4203(90)90059-L, 1990.

673 Arnold, S. R., Spracklen, D. V., Gebhardt, S., Custer, T., Williams, J., Peeken, I., and Alvaín, S.: Relationships between
674 atmospheric organic compounds and air-mass exposure to marine biology, *Environ. Chem.*, 7, 232-241, 10.1071/en09144,
675 2010.

676 Aurin, D. A., and Dierssen, H. M.: Advantages and limitations of ocean color remote sensing in CDOM-dominated, mineral-
677 rich coastal and estuarine waters, *Remote Sensing of Environment*, 125, 181-197, 10.1016/j.rse.2012.07.001, 2012.

678 Barnes, I., Hjorth, J., and Mihalopoulos, N.: Dimethyl sulfide and dimethyl sulfoxide and their oxidation in the atmosphere,
679 *Chem. Rev.*, 106, 940-975, 10.1021/cr020529+, 2006.

680 Bates, T. S., Calhoun, J. A., and Quinn, P. K.: Variations in the Methanesulfonate to Sulfate Molar Ratio in Submicrometer
681 Marine Aerosol-Particles over the South-Pacific Ocean, *J. Geophys. Res.-Atmos.*, 97, 9859-9865, 10.1029/92JD00411, 1992.

682 Beale, R., Johnson, M., Liss, P. S., and Nightingale, P. D.: Air-Sea Exchange of Marine Trace Gases, in: *Treatise on*
683 *Geochemistry (Second Edition)*, edited by: Holland, H. D., and Turekian, K. K., 2, Elsevier, Oxford, 53-92, 2014.

684 Behrenfeld, M. J., Moore, R. H., Hostetler, C. A., Graff, J., Gaube, P., Russell, L. M., Chen, G., Doney, S. C., Giovannoni, S.,
685 Liu, H., Proctor, C., Bolaños, L. M., Baetge, N., Davie-Martin, C., Westberry, T. K., Bates, T. S., Bell, T. G., Bidle, K. D.,

686 Boss, E. S., Brooks, S. D., Cairns, B., Carlson, C., Halsey, K., Harvey, E. L., Hu, C., Karp-Boss, L., Kleb, M., Menden-Deuer,
687 S., Morison, F., Quinn, P. K., Scarino, A. J., Anderson, B., Chowdhary, J., Crosbie, E., Ferrare, R., Hair, J. W., Hu, Y., Janz,

688 S., Redemann, J., Saltzman, E., Shook, M., Siegel, D. A., Wisthaler, A., Martin, M. Y., and Ziemba, L.: The North Atlantic
689 Aerosol and Marine Ecosystem Study (NAAMES): Science Motive and Mission Overview, *Front. Mar. Sci.*, 6,

690 10.3389/fmars.2019.00122, 2019.

691 Bell, T. G., Porter, J. G., Wang, W.-L., Lawler, M. J., Boss, E., Behrenfeld, M. J., and Saltzman, E. S.: Predictability of
692 Seawater DMS During the North Atlantic Aerosol and Marine Ecosystem Study (NAAMES), *Front. Mar. Sci.*, 7, 596763,
693 10.3389/fmars.2020.596763, 2021.

694 Belviso, S., Bopp, L., Moulin, C., Orr, J. C., Anderson, T. R., Aumont, O., Chu, S., Elliott, S., Maltrud, M. E., and Simó, R.:
695 Comparison of global climatological maps of sea surface dimethyl sulfide, *Glob. Biogeochem. Cycles*, 18,
696 10.1029/2003gb002193, 2004a.

697 Belviso, S., Moulin, C., Bopp, L., and Stefels, J.: Assessment of a global climatology of oceanic dimethylsulfide (DMS)
698 concentrations based on SeaWiFS imagery (1998-2001), *Canadian Journal of Fisheries and Aquatic Sciences*, 61, 804-816,
699 10.1139/f04-001, 2004b.

700 Belviso, S., Masotti, I., Tagliabue, A., Bopp, L., Brockmann, P., Fichot, C., Caniaux, G., Prieur, L., Ras, J., Uitz, J., Loisel,
701 H., Dessailly, D., Alvain, S., Kasamatsu, N., and Fukuchi, M.: DMS dynamics in the most oligotrophic subtropical zones of
702 the global ocean, *Biogeochemistry*, 110, 215-241, 10.1007/s10533-011-9648-1, 2011.

703 Bergen, K. J., Johnson, P. A., de Hoop, M. V., and Beroza, G. C.: Machine learning for data-driven discovery in solid Earth
704 geoscience, *Science*, 363, eaau0323, 10.1126/science.aau0323, 2019.

705 Carslaw, K. S., Lee, L. A., Reddington, C. L., Pringle, K. J., Rap, A., Forster, P. M., Mann, G. W., Spracklen, D. V.,
706 Woodhouse, M. T., Regayre, L. A., and Pierce, J. R.: Large contribution of natural aerosols to uncertainty in indirect forcing,
707 *Nature*, 503, 67-71, 10.1038/nature12674, 2013.

708 Charlson, R. J., Lovelock, J. E., Andreaei, M. O., and Warren, S. G.: Oceanic phytoplankton, atmospheric sulphur, cloud
709 albedo and climate, *Nature*, 326, 655-661, 10.1038/326655a0, 1987.

710 Chen, Q., Sherwen, T., Evans, M., and Alexander, B.: DMS oxidation and sulfur aerosol formation in the marine troposphere:
711 a focus on reactive halogen and multiphase chemistry, *Atmos. Chem. Phys.*, 18, 13617-13637, 10.5194/acp-18-13617-2018,
712 2018.

713 Dubitzky, W., Granzow, M., and Berrar, D. P.: *Fundamentals of data mining in genomics and proteomics*, Springer Science
714 & Business Media, 2007.

715 Forget, G., Campin, J.-M., Heimbach, P., Hill, C. N., Ponte, R. M., and Wunsch, C.: ECCO version 4: An integrated framework
716 for non-linear inverse modeling and global ocean state estimation, *Geosci. Model Dev.*, 8, 3071-3104, 2015.

717 Friedland, K. D., Mouw, C. B., Asch, R. G., Ferreira, A. S. A., Henson, S., Hyde, K. J. W., Morse, R. E., Thomas, A. C., and
718 Brady, D. C.: Phenology and time series trends of the dominant seasonal phytoplankton bloom across global scales, *Global
719 Ecology and Biogeography*, 27, 551-569, 10.1111/geb.12717, 2018.

720 Fung, K. M., Heald, C. L., Kroll, J. H., Wang, S., Jo, D. S., Gettelman, A., Lu, Z., Liu, X., Zaveri, R. A., Apel, E. C., Blake,
721 D. R., Jimenez, J. L., Campuzano-Jost, P., Veres, P. R., Bates, T. S., Shilling, J. E., and Zawadowicz, M.: Exploring dimethyl
722 sulfide (DMS) oxidation and implications for global aerosol radiative forcing, *Atmos. Chem. Phys.*, 22, 1549-1573,
723 10.5194/acp-22-1549-2022, 2022.

724 Galí, M., Devred, E., Levasseur, M., Royer, S.-J., and Babin, M.: A remote sensing algorithm for planktonic
725 dimethylsulfoniopropionate (DMSP) and an analysis of global patterns, *Remote Sensing of Environment*, 171, 171-184,
726 10.1016/j.rse.2015.10.012, 2015.

727 Galí, M., and Simó, R.: A meta-analysis of oceanic DMS and DMSP cycling processes: Disentangling the summer paradox,
728 *Glob. Biogeochem. Cycles*, 29, 496-515, 10.1002/2014gb004940, 2015.

729 Galí, M., Levasseur, M., Devred, E., Simó, R., and Babin, M.: Sea-surface dimethylsulfide (DMS) concentration from satellite
730 data at global and regional scales, *Biogeosciences*, 15, 3497-3519, 10.5194/bg-15-3497-2018, 2018.

731 Galí, M., Devred, E., Babin, M., and Levasseur, M.: Decadal increase in Arctic dimethylsulfide emission, *P. Natl. Acad. Sci.*
732 *USA*, 116, 19311-19317, 10.1073/pnas.1904378116, 2019.

733 Garcia, H., Weathers, K., Paver, C., Smolyar, I., Boyer, T., Locarnini, M., Zweng, M., Mishonov, A., Baranova, O., and Seidov,
734 D.: *World ocean atlas 2018. Vol. 4: Dissolved inorganic nutrients (phosphate, nitrate and nitrate+ nitrite, silicate)*. A. Mishonov
735 Technical Ed.; NOAA Atlas NESDIS 84, 35 pp., 2019a.

736 Garcia, H., Weathers, K., Paver, C., Smolyar, I., Boyer, T., Locarnini, M., Zweng, M., Mishonov, A., Baranova, O., and Seidov,
737 D.: *World Ocean Atlas 2018, Volume 3: Dissolved Oxygen, Apparent Oxygen Utilization, and Dissolved Oxygen Saturation*.
738 A. Mishonov Technical Ed.; NOAA Atlas NESDIS 83, 38 pp., 2019b.

739 Garnesson, P., Mangin, A., Fanton d'Andon, O., Demaria, J., and Bretagnon, M.: The CMEMS GlobColour chlorophyll a
740 product based on satellite observation: Multi-sensor merging and flagging strategies, *Ocean Science*, 15, 819-830, 2019.

741 Hoffmann, E. H., Tilgner, A., Schroedner, R., Bräuer, P., Wolke, R., and Herrmann, H.: An advanced modeling study on the
742 impacts and atmospheric implications of multiphase dimethyl sulfide chemistry, *P. Natl. Acad. Sci. USA*, 113, 11776-11781,
743 10.1073/pnas.1606320113, 2016.

744 Holder, C., Gnanadesikan, A., and Aude-Pradal, M.: Using neural network ensembles to separate ocean biogeochemical and
745 physical drivers of phytoplankton biogeography in Earth system models, *Geosci. Model Dev.*, 15, 1595-1617, 10.5194/gmd-
746 15-1595-2022, 2022.

747 Hopkins, F. E., Turner, S. M., Nightingale, P. D., Steinke, M., Bakker, D., and Liss, P. S.: Ocean acidification and marine
748 trace gas emissions, *P. Natl. Acad. Sci. USA*, 107, 760-765, 10.1073/pnas.0907163107, 2010.

749 Hopkins, F. E., Archer, S. D., Bell, T. G., Suntharalingam, P., and Todd, J. D.: The biogeochemistry of marine dimethylsulfide,
750 *Nature Reviews Earth & Environment*, 4, 361-376, 10.1038/s43017-023-00428-7, 2023.

751 Huang, B., Liu, C., Freeman, E., Graham, G., Smith, T., and Zhang, H.-M.: Assessment and Intercomparison of NOAA Daily
752 Optimum Interpolation Sea Surface Temperature (DOISST) Version 2.1, *Journal of Climate*, 34, 7421-7441, 10.1175/jcli-d-
753 21-0001.1, 2021.

754 Huang, S., Poulain, L., van Pinxteren, D., van Pinxteren, M., Wu, Z., Herrmann, H., and Wiedensohler, A.: Latitudinal and
755 Seasonal Distribution of Particulate MSA over the Atlantic using a Validated Quantification Method with HR-ToF-AMS,
756 *Environ. Sci. Technol.*, 51, 418-426, 10.1021/acs.est.6b03186, 2016.

757 Hulswar, S., Simó, R., Galí, M., Bell, T. G., Lana, A., Inamdar, S., Halloran, P. R., Manville, G., and Mahajan, A. S.: Third
758 revision of the global surface seawater dimethyl sulfide climatology (DMS-Rev3), *Earth System Science Data*, 14, 2963-2987,
759 10.5194/essd-14-2963-2022, 2022.

760 Humphries, G. R. W., Deal, C. J., Elliott, S., and Huettmann, F.: Spatial predictions of sea surface dimethylsulfide
761 concentrations in the high arctic, *Biogeochemistry*, 110, 287-301, 2012.

762 Johnson, M. T.: A numerical scheme to calculate temperature and salinity dependent air-water transfer velocities for any gas,
763 *Ocean Sci.*, 6, 913-932, 10.5194/os-6-913-2010, 2010.

764 Keller, M. D., Bellows, W. K., and Guillard, R. R.: Dimethyl sulfide production in marine phytoplankton, in: *Biogenic Sulfur*
765 *in the Environment*, edited by: Saltzman, E. S., and Cooper, W. J., ACS Publications, 1989.

766 Kettle, A. J., Andreae, M. O., Amouroux, D., Andreae, T. W., Bates, T. S., Berresheim, H., Bingemer, H., Boniforti, R., Curran,
767 M. A. J., DiTullio, G. R., Helas, G., Jones, G. B., Keller, M. D., Kiene, R. P., Leck, C., Lévassieur, M., Malin, G., Maspero,
768 M., Matrai, P., McTaggart, A. R., Mihalopoulos, N., Nguyen, B. C., Novo, A., Putaud, J. P., Rapsomanikis, S., Roberts, G.,
769 Schebeske, G., Sharma, S., Simo, R., Staubes, R., Turner, S., and Uher, G.: A global database of sea surface dimethylsulfide
770 (DMS) measurements and a procedure to predict sea surface DMS as a function of latitude, longitude, and month, *Glob.*
771 *Biogeochem. Cycles*, 13, 399-444, 10.1029/1999gb900004, 1999.

772 Kloster, S., Feichter, J., Maier-Reimer, E., Six, K. D., Stier, P., and Wetzel, P.: DMS cycle in the marine ocean-atmosphere
773 system—a global model study, *Biogeosciences*, 3, 29-51, 2006.

774 Lana, A., Bell, T. G., Simó, R., Vallina, S. M., Ballabrera-Poy, J., Kettle, A. J., Dachs, J., Bopp, L., Saltzman, E. S., Stefels,
775 J., Johnson, J. E., and Liss, P. S.: An updated climatology of surface dimethylsulfide concentrations and emission fluxes in the
776 global ocean, *Glob. Biogeochem. Cycles*, 25, GB1004, 10.1029/2010gb003850, 2011.

777 Li, H., Zhou, S., Zhu, Y., Zhang, R., Wang, F., Bao, Y., and Chen, Y.: Atmospheric Deposition Promotes Relative Abundances
778 of High-Dimethylsulfoniopropionate Producers in the Western North Pacific, *Geophys. Res. Lett.*, 48, e2020GL092077,
779 10.1029/2020GL092077, 2021.

780 Longhurst, A. R.: *Ecological Geography of the Sea*, Academic Press, 1998.

781 Lovelock, J. E., Maggs, R. J., and Rasmussen, R. A.: Atmospheric Dimethyl Sulphide and the Natural Sulphur Cycle, *Nature*,
782 237, 452-453, 10.1038/237452a0, 1972.

783 Mansour, K., Decesari, S., Ceburnis, D., Ovadnevaite, J., and Rinaldi, M.: Machine learning for prediction of daily sea surface
784 dimethylsulfide concentration and emission flux over the North Atlantic Ocean (1998-2021), *Sci. Total. Environ.*, 871, 162123,
785 10.1016/j.scitotenv.2023.162123, 2023.

786 Masson-Delmotte, V., Zhai, P., Pirani, A., Connors, S. L., Péan, C., Berger, S., Caud, N., Chen, Y., Goldfarb, L., Gomis, M.
787 I., Huang, M., Leitzell, K., Lonnoy, E., Matthews, J. B. R., Maycock, T. K., Waterfield, T., Yelekçi, O., Yu, R., and Zhou, R.
788 e.: IPCC, 2021: *Climate Change 2021: The Physical Science Basis*. Contribution of Working Group I to the Sixth Assessment
789 Report of the Intergovernmental Panel on Climate Change, 2021.

790 McCoy, D. T., Burrows, S. M., Wood, R., Grosvenor, D. P., Elliott, S. M., Ma, P. L., Rasch, P. J., and Hartmann, D. L.: Natural
791 aerosols explain seasonal and spatial patterns of Southern Ocean cloud albedo, *Science Advances*, 1, e1500157,
792 10.1126/sciadv.1500157, 2015.

793 McNabb, B. J., and Tortell, P. D.: Improved prediction of dimethyl sulfide (DMS) distributions in the northeast subarctic
794 Pacific using machine-learning algorithms, *Biogeosciences*, 19, 1705-1721, 10.5194/bg-19-1705-2022, 2022.

795 McNabb, B. J., and Tortell, P. D.: Oceanographic controls on Southern Ocean dimethyl sulfide distributions revealed by
796 machine learning algorithms, *Limnology and Oceanography*, 68, 616-630, 10.1002/lno.12298, 2023.

797 McParland, E. L., and Levine, N. M.: The role of differential DMSP production and community composition in predicting
798 variability of global surface DMSP concentrations, *Limnol. Oceanogr.*, 64, 757-773, 10.1002/lno.11076, 2018.

799 Moradkhani, H., DeChant, C. M., and Sorooshian, S.: Evolution of ensemble data assimilation for uncertainty quantification
800 using the particle filter-Markov chain Monte Carlo method, *Water Resources Research*, 48, 10.1029/2012wr012144, 2012.

801 Nightingale, P. D., Malin, G., Law, C. S., Watson, A. J., Liss, P. S., Liddicoat, M. I., Boutin, J., and Upstill-Goddard, R. C.:
802 In situ evaluation of air-sea gas exchange parameterizations using novel conservative and volatile tracers, *Glob. Biogeochem.*
803 *Cycles*, 14, 373-387, 10.1029/1999gb900091, 2000.

804 Novak, G. A., Fite, C. H., Holmes, C. D., Veres, P. R., Neuman, J. A., Faloon, I., Thornton, J. A., Wolfe, G. M., Vermeuel,
805 M. P., Jernigan, C. M., Peischl, J., Ryerson, T. B., Thompson, C. R., Bourgeois, I., Warneke, C., Gkatzelis, G. I., Coggon, M.
806 M., Sekimoto, K., Bui, T. P., Dean-Day, J., Diskin, G. S., DiGangi, J. P., Nowak, J. B., Moore, R. H., Wiggins, E. B., Winstead,
807 E. L., Robinson, C., Thornhill, K. L., Sanchez, K. J., Hall, S. R., Ullmann, K., Dollner, M., Weinzierl, B., Blake, D. R., and
808 Bertram, T. H.: Rapid cloud removal of dimethyl sulfide oxidation products limits SO₂ and cloud condensation nuclei
809 production in the marine atmosphere, *P. Natl. Acad. Sci. USA*, 118, e2110472118, 10.1073/pnas.2110472118, 2021.

810 Omori, Y., Tanimoto, H., Inomata, S., Wada, S., Thume, K., and Pohnert, G.: Enhancement of dimethylsulfide production by
811 anoxic stress in natural seawater, *Geophys. Res. Lett.*, 42, 4047-4053, 10.1002/2015gl063546, 2015.

812 Osman, M. B., Das, S. B., Trusel, L. D., Evans, M. J., Fischer, H., Grieman, M. M., Kipfstuhl, S., McConnell, J. R., and
813 Saltzman, E. S.: Industrial-era decline in subarctic Atlantic productivity, *Nature*, 569, 551-555, 10.1038/s41586-019-1181-8,
814 2019.

815 Park, K.-T., Lee, K., Kim, T.-W., Yoon, Y. J., Jang, E.-H., Jang, S., Lee, B.-Y., and Hermansen, O.: Atmospheric DMS in the
816 Arctic Ocean and Its Relation to Phytoplankton Biomass, *Glob. Biogeochem. Cycles*, 32, 351-359, 10.1002/2017gb005805,
817 2018.

818 Park, K. T., Yoon, Y. J., Lee, K., Tunved, P., Krejci, R., Ström, J., Jang, E., Kang, H. J., Jang, S., Park, J., Lee, B. Y., Traversi,
819 R., Becagli, S., and Hermansen, O.: Dimethyl Sulfide-Induced Increase in Cloud Condensation Nuclei in the Arctic
820 Atmosphere, *Glob. Biogeochem. Cycles*, 35, e2021GB006969, 10.1029/2021gb006969, 2021.

821 Qu, B., Gabric, A. J., Zeng, M., and Lu, Z.: Dimethylsulfide model calibration in the Barents Sea using a genetic algorithm
822 and neural network, *Environ. Chem.*, 13, 413-424, 10.1071/EN14264, 2016.

823 Quinn, P. K., and Bates, T. S.: The case against climate regulation via oceanic phytoplankton sulphur emissions, *Nature*, 480,
824 51-56, 10.1038/nature10580, 2011.

825 Quinn, P. K., Coffman, D. J., Johnson, J. E., Upchurch, L. M., and Bates, T. S.: Small fraction of marine cloud condensation
826 nuclei made up of sea spray aerosol, *Nat. Geosci.*, 10, 674-679, 10.1038/ngeo3003, 2017.

827 Reichstein, M., Camps-Valls, G., Stevens, B., Jung, M., Denzler, J., Carvalhais, N., and Prabhat: Deep learning and process
828 understanding for data-driven Earth system science, *Nature*, 566, 195-204, 10.1038/s41586-019-0912-1, 2019.

829 Saltzman, E. S., Savoie, D. L., Zika, R. G., and Prospero, J. M.: Methane sulfonic acid in the marine atmosphere, *J. Geophys.*
830 *Res.*, 88, 10897, 10.1029/JC088iC15p10897, 1983.

831 Savoie, D. L., Arimoto, R., Keene, W. C., Prospero, J. M., Duce, R. A., and Galloway, J. N.: Marine biogenic and
832 anthropogenic contributions to non-sea-salt sulfate in the marine boundary layer over the North Atlantic Ocean, *J. Geophys.*
833 *Res.*, 107, 4356, 10.1029/2001jd000970, 2002.

834 Screen, J. A., Deser, C., and Simmonds, I.: Local and remote controls on observed Arctic warming, *Geophys. Res. Lett.*, 39,
835 L10709, 10.1029/2012gl051598, 2012.

836 Serreze, M. C., and Barry, R. G.: Processes and impacts of Arctic amplification: A research synthesis, *Global and planetary*
837 *change*, 77, 85-96, 2011.

838 Sheng, J.-X., Weisenstein, D. K., Luo, B.-P., Rozanov, E., Stenke, A., Anet, J., Bingemer, H., and Peter, T.: Global atmospheric
839 sulfur budget under volcanically quiescent conditions: Aerosol-chemistry-climate model predictions and validation, *J.*
840 *Geophys. Res.-Atmos.*, 120, 256-276, 10.1002/2014jd021985, 2015.

841 Sigmund, G., Gharasoo, M., Hüffer, T., and Hofmann, T.: Deep Learning Neural Network Approach for Predicting the
842 Sorption of Ionizable and Polar Organic Pollutants to a Wide Range of Carbonaceous Materials, *Environ. Sci. Technol.*, 54,
843 4583-4591, 10.1021/acs.est.9b06287, 2020.

844 Simó, R., and Pedrós-Alió, C.: Role of vertical mixing in controlling the oceanic production of dimethyl sulphide, *Nature*, 402,
845 396-399, 10.1038/46516, 1999a.

846 Simó, R., and Pedrós-Alió, C.: Short-term variability in the open ocean cycle of dimethylsulfide, *Glob. Biogeochem. Cycles*,
847 13, 1173-1181, 10.1029/1999gb900081, 1999b.

848 Simó, R., and Dachs, J.: Global ocean emission of dimethylsulfide predicted from biogeophysical data, *Glob. Biogeochem.*
849 *Cycles*, 16, 1078, 10.1029/2001gb001829, 2002.

850 Six, K. D., Kloster, S., Ilyina, T., Archer, S. D., Zhang, K., and Maier-Reimer, E.: Global warming amplified by reduced
851 sulphur fluxes as a result of ocean acidification, *Nat. Clim. Change*, 3, 975-978, 10.1038/nclimate1981, 2013.

852 Stefels, J.: Physiological aspects of the production and conversion of DMSP in marine algae and higher plants, *J. Sea. Res.*,
853 43, 183-197, 2000.

854 Stefels, J., Steinke, M., Turner, S., Malin, G., and Belviso, S.: Environmental constraints on the production and removal of the
855 climatically active gas dimethylsulphide (DMS) and implications for ecosystem modelling, *Biogeochemistry*, 83, 245-275,
856 10.1007/s10533-007-9091-5, 2007.

857 Stein, A. F., Draxler, R. R., Rolph, G. D., Stunder, B. J. B., Cohen, M. D., and Ngan, F.: NOAA's HYSPLIT Atmospheric
858 Transport and Dispersion Modeling System, *B. Am. Meteorol. Soc.*, 96, 2059-2077, 10.1175/bams-d-14-00110.1, 2015.

859 Steiner, N. S., Robert, M., Arychuk, M., Levasseur, M. L., Merzouk, A., Peña, M. A., Richardson, W. A., and Tortell, P. D.:
860 Evaluating DMS measurements and model results in the Northeast subarctic Pacific from 1996–2010, *Biogeochemistry*, 110,
861 269-285, 10.1007/s10533-011-9669-9, 2011.

862 Sunda, W., Kieber, D., Kiene, R., and Huntsman, S.: An antioxidant function for DMSP and DMS in marine algae, *Nature*,
863 418, 317-320, 2002.

864 Tesdal, J.-E., Christian, J. R., Monahan, A. H., and Salzen, K. v.: Evaluation of diverse approaches for estimating sea-surface
865 DMS concentration and air–sea exchange at global scale, *Environ. Chem.*, 13, 390-412, 10.1071/EN14255, 2016.

866 Vallina, S. M., and Simó, R.: Strong relationship between DMS and the solar radiation dose over the global surface ocean,
867 *Science*, 315, 506-508, 10.1126/science.1133680, 2007.

868 Vogt, M., Vallina, S. M., Buitenhuis, E. T., Bopp, L., and Le Quéré, C.: Simulating dimethylsulphide seasonality with the
869 Dynamic Green Ocean Model PlankTOM5, *J. Geophys. Res.*, 115, 10.1029/2009jc005529, 2010.

870 Wang, S., Elliott, S., Maltrud, M., and Cameron-Smith, P.: Influence of explicit Phaeocystis parameterizations on the global
871 distribution of marine dimethyl sulfide, *J. Geophys. Res.-Biogeosci.*, 120, 2158-2177, 10.1002/2015jg003017, 2015.

872 Wang, W.-L., Song, G., Primeau, F., Saltzman, E. S., Bell, T. G., and Moore, J. K.: Global ocean dimethyl sulfide climatology
873 estimated from observations and an artificial neural network, *Biogeosciences*, 17, 5335-5354, 10.5194/bg-17-5335-2020, 2020.

874 Wood, R., Stemmler, J. D., Rémillard, J., and Jefferson, A.: Low-CCN concentration air masses over the eastern North Atlantic:
875 Seasonality, meteorology, and drivers, *Journal of Geophysical Research: Atmospheres*, 122, 1203-1223,
876 10.1002/2016jd025557, 2017.

877 Woolf, D. K.: Bubbles and their role in gas exchange, in: *The Sea Surface and Global Change*, edited by: Liss, P. S., and Duce,
878 R. A., Cambridge University Press, Cambridge, 173-206, 1997.

879 Yang, B., Boss, E. S., Haëntjens, N., Long, M. C., Behrenfeld, M. J., Eveleth, R., and Doney, S. C.: Phytoplankton Phenology
880 in the North Atlantic: Insights From Profiling Float Measurements, *Front. Mar. Sci.*, 7, 10.3389/fmars.2020.00139, 2020.

881 Zhang, X. H., Liu, J., Liu, J., Yang, G., Xue, C. X., Curson, A. R. J., and Todd, J. D.: Biogenic production of DMSP and its
882 degradation to DMS-their roles in the global sulfur cycle, *Sci. China Life Sci.*, 62, 1296-1319, 10.1007/s11427-018-9524-y,
883 2019.

884 Zhao, J., Ma, W., Bilsback, K. R., Pierce, J. R., Zhou, S., Chen, Y., Yang, G., and Zhang, Y.: Simulating the radiative forcing
885 of oceanic dimethylsulfide (DMS) in Asia based on machine learning estimates, *Atmos. Chem. Phys.*, 22, 9583-9600,
886 10.5194/acp-22-9583-2022, 2022.

887 Zheng, G., Li, X., Zhang, R. H., and Liu, B.: Purely satellite data-driven deep learning forecast of complicated tropical
888 instability waves, *Science Advances*, 6, eaba1482, 10.1126/sciadv.aba1482, 2020.

889 Zhou, S.: An artificial neural network ensemble model for sea surface DMS simulation, v2.0, Zenodo [Data set],
890 <https://doi.org/10.5281/zenodo.10937598>, 2024

891 Zhou, S., Chen, Y., Huang, S., Gong, X., Yang, G., Zhang, H., Herrmann, H., Wiedensohler, A., Poulain, L., Zhang, Y., Wang,
892 F., Xu, Z., and Yan, K.: A 20-year (1998-2017) global sea surface dimethyl sulfide gridded dataset with daily resolution, v3.0,
893 810 Zenodo [Data set], <https://doi.org/10.5281/zenodo.10906101>, 2024.

894 Zhou, S., Chen, Y., Paytan, A., Li, H., Wang, F., Zhu, Y., Yang, T., Zhang, Y., and Zhang, R.: Non-Marine Sources Contribute
895 to Aerosol Methanesulfonate Over Coastal Seas, *J. Geophys. Res.-Atmos.*, 126, e2021JD034960, 10.1029/2021jd034960,
896 2021.

897 Zindler, C., Bracher, A., Marandino, C. A., Taylor, B., Torrecilla, E., Kock, A., and Bange, H. W.: Sulphur compounds,
898 methane, and phytoplankton: interactions along a north–south transit in the western Pacific Ocean, *Biogeosciences*, 10, 3297-
899 3311, 10.5194/bg-10-3297-2013, 2013.

900 Zindler, C., Marandino, C. A., Bange, H. W., Schütte, F., and Saltzman, E. S.: Nutrient availability determines dimethyl sulfide
901 and isoprene distribution in the eastern Atlantic Ocean, *Geophys. Res. Lett.*, 41, 3181-3188, 10.1002/2014gl059547, 2014.
902